

UPPSALA UNIVERSITY

Electronic structures of transition metal  
complexes-core level spectroscopic  
investigation

by

Meiyuan Guo



UPPSALA  
UNIVERSITET

Dissertation for the Licentiate of Philosophy in Quantum Chemistry

in the

Disciplinary Domain of Science and Technology  
Department of Chemistry-Ångström Laboratory

February 2016



*“The failures and reverses which await men  
and one after another sadden the brow of  
youth—add a dignity to the prospect of  
human life, which no Arcadian success would do.”*

*Henry David Thoreau*

UPPSALA UNIVERSITY

## *Abstract*

Disciplinary Domain of Science and Technology  
Department of Chemistry-Ångström Laboratory

by Meiyuan Guo

Probing the unoccupied and partially occupied metal  $3d$  character orbitals involved in catalysis makes it possible to identify and characterize the reactive sites, e.g., site symmetry, oxidation state and ligand-field splitting. The metal L-edge ( $2p \rightarrow 3d$ ), K pre-edge ( $1s \rightarrow 3d$ ) X-ray absorption spectra (XAS) and  $1s2p$  ( $1s \rightarrow 3d$  followed by  $2p \rightarrow 1s$ ) resonant inelastic X-ray scattering (RIXS) spectra can all be used to investigate the metal  $3d$  orbitals. Here, the restricted active space (RAS) method is used to successfully reproduce different types of X-ray spectra by including all important spectral effects: multiplet structures, spin-orbit coupling (SOC), charge-transfer excitations, ligand field splitting and  $3d - 4p$  orbital hybridization. In this thesis, the K pre-edge spectra of centrosymmetric complexes  $[FeCl_6]^{n-}$  in ferrous and ferric oxidation states are discussed as  $\sigma$  and  $\pi$  donor model systems, and it is shown that the multiplet structures are well described. The intensity of the K pre-edge increases significantly if the centrosymmetric environment is broken, e.g., when going from a six-coordinate to the four-coordinate site in  $[FeCl_4]^{n-}$ . Distortions from centrosymmetry allow for  $3d - 4p$  orbital hybridization, which gives rise to dipole-allowed transitions in the K pre-edge region. The iron complexes  $[Fe(CN)_6]^{n-}$  are adopted as  $\pi$  back-donation model systems, its back-donation charge transfer feature is reproduced both in metal L-edge and K pre-edge XAS. The RAS method is extended to simulate the two-photon  $1s2p$  RIXS process of  $[Fe(CN)_6]^{n-}$  in ferrous and ferric oxidation states. The spectra can deliver ample electronic details with high resolution. To gain further chemical insight, the origins of the spectral features have been analyzed with a chemically intuitive molecular orbital picture that serves as a bridge between the spectra and the electronic structures. These simulations make RAS an attractive method for modeling and interpreting XAS and RIXS spectra of many small and medium-sized transition metal catalysts.

# List of Publications

This licentiate thesis is based on the following papers:

**I Restricted active space calculations of L-edge X-ray absorption spectra:  
From molecular orbitals to multiplet states**

Rahul V Pinjari, Mickaël G Delcey, Meiyuan Guo, Michael Odellius and Marcus Lundberg. *J. Chem. Phys.*, 141,124116 (2014), DOI: [10.1063/1.4896373](https://doi.org/10.1063/1.4896373)

**II Cost and sensitivity of restricted active space calculations of metal L-edge X-ray absorption spectra**

Rahul V Pinjari, Mickaël G Delcey, Meiyuan Guo, Michael Odellius and Marcus Lundberg. *J. Comput. Chem.*, 37, 477 (2016), DOI: [10.1002/jcc.24237](https://doi.org/10.1002/jcc.24237)

**III Simulations of iron K pre-edge X-ray absorption spectra using the restricted active space method**

Meiyuan Guo, Lasse Kragh Sørensen, Mickaël G Delcey, Rahul V Pinjari and Marcus Lundberg. *Phys. Chem. Chem. Phys.*, 18, 3250 (2016), DOI: [10.1039/C5CP07487H](https://doi.org/10.1039/C5CP07487H)

**IV Molecular orbital simulations of metal 1s2p resonant inelastic X-ray scattering**

Meiyuan Guo, Erik, Källman, Lasse Kragh Sørensen, Mickaël G Delcey, Rahul V Pinjari and Marcus Lundberg. manuscript



# Comments on my own contribution

- I Performed the multiplet calculations, took part in analysing the results and writing the manuscript.
- II Performed the calculations of convergence dependence on the number of final states, RASPT2 calculations with correlated core orbitals and took part in analysing the results.
- III Participated in the design of the study, performed all calculations, analysis, and had the main responsibility for writing of the manuscript.
- IV Participated in the design of the study, had the main responsibility for the calculations, and the analysis.



# Abbreviations

<b>IP</b>	<b>I</b> onisation <b>P</b> otential
<b>HF</b>	<b>H</b> artree- <b>F</b> ock
<b>MCSCF</b>	<b>M</b> ulti- <b>C</b> <b>S</b> elf <b>C</b> onsistent field
<b>MO</b>	<b>M</b> olecular <b>O</b> rbitals
<b>TP</b>	<b>T</b> ransition <b>P</b> otential
<b>RAS</b>	<b>R</b> estricted <b>A</b> ctive <b>S</b> pace
<b>RASSI</b>	<b>R</b> estricted <b>a</b> ctive <b>S</b> pace <b>S</b> tate <b>I</b> nteraction
<b>CAS</b>	<b>C</b> omplete <b>A</b> ctive <b>S</b> pace
<b>XAS</b>	<b>X</b> -ray <b>A</b> bsorption <b>S</b> pectroscopy
<b>RIXS</b>	<b>R</b> esonant <b>I</b> nelastic <b>X</b> -ray <b>S</b> cattering
<b>CI</b>	<b>C</b> onfiguration <b>I</b> nteraction
<b>SCF</b>	<b>S</b> elf- <b>C</b> onsistent <b>F</b> ield
<b>DFT</b>	<b>D</b> ensity <b>F</b> unctional <b>T</b> heory
<b>TD</b>	<b>T</b> ime <b>D</b> ependent
<b>CTM</b>	<b>C</b> harge <b>T</b> ransfer <b>M</b> ultiplet
<b>SOC</b>	<b>S</b> pin <b>O</b> rbital <b>C</b> oupling
<b>MC</b>	<b>M</b> ulti- <b>C</b> onfiguration
<b>PT2</b>	<b>S</b> econd-order <b>P</b> erturbation <b>T</b> heory
<b>LMCT</b>	<b>L</b> igand <b>M</b> etal <b>C</b> harge <b>T</b> ransfer
<b>MLCT</b>	<b>M</b> etal <b>L</b> igand <b>C</b> harge <b>T</b> ransfer
<b>MAD</b>	<b>M</b> ean <b>A</b> bsolute <b>D</b> eviation
<b>ROCIS</b>	<b>R</b> estricted- <b>O</b> pen <b>S</b> hell <b>C</b> onfiguration <b>I</b> nteraction with <b>S</b> ingles
<b>EPR</b>	<b>E</b> lectron <b>P</b> aramagnetic <b>R</b> esonance
<b>MCD</b>	<b>M</b> agnetic <b>c</b> ircular <b>D</b> ichroism
<b>RR</b>	<b>R</b> esonance <b>R</b> aman (RR)
<b>MS</b>	<b>M</b> ulti- <b>S</b> tate
<b>SA</b>	<b>S</b> tate <b>A</b> verage
<b>CIE</b>	<b>C</b> onstant <b>I</b> ncident <b>E</b> nergy
<b>CEE</b>	<b>C</b> onstant <b>E</b> mission <b>E</b> nergy



# Contents

<b>List of Publications</b>	<b>v</b>
<b>Comments on my own contribution</b>	<b>vii</b>
<b>Abbreviations</b>	<b>vii</b>
<b>1 Introduction</b>	<b>1</b>
<b>2 Computational framework</b>	<b>7</b>
2.1 Born-Oppenheimer approximation . . . . .	7
2.2 Hartree-Fock theory . . . . .	9
2.3 Multi-configurational method . . . . .	10
2.3.1 Second-order perturbation . . . . .	11
2.3.2 RAS method for X-ray spectra . . . . .	12
2.3.3 Orbital contribution analysis . . . . .	14
2.4 Charge transfer multiplet model . . . . .	15
<b>3 Simulation of the metal L-edge XAS</b>	<b>17</b>
3.1 Atomic calculation of $Fe^{3+}$ . . . . .	17
3.2 Metal L-edges of low spin $[Fe(CN)_6]^{3-}$ . . . . .	20
<b>4 Simulation of the metal K pre-edge XAS</b>	<b>23</b>
4.1 Multiplet structure . . . . .	23
4.2 Hybridization of dipole and quadrupole contributions . . . . .	26
4.3 Back-donation charge transfer . . . . .	27
<b>5 Simulation of the 1s2p RIXS</b>	<b>29</b>
5.1 The 1s2p RIXS spectrum of $[Fe(CN)_6]^{4-}$ . . . . .	30
5.2 The 1s2p RIXS spectrum of $[Fe(CN)_6]^{3-}$ . . . . .	31
<b>6 Conclusion</b>	<b>33</b>
<b>Bibliography</b>	<b>35</b>
<b>Acknowledgements</b>	<b>35</b>



# Chapter 1

## Introduction

The increasing demand of energy boosts the consumption of coal, oil, and natural gas, which in turn boosts the emission of carbon dioxide and other greenhouse gases. These energy sources have limited reserves and will dwindle in the foreseeable future, and the consumptions are adversely affecting our environment and human health. The urgent circumstance forces us to find alternative green energies, such as hydro, biofuels, geothermal, wind, and solar energy, *etc.* Among all of these green energies, solar energy is the most attractive alternative energy source and can replace fossil fuels.[1]

The natural photosynthetic process occurring in plant and algae shows us a perfect example how to utilize the solar energy. During the photosynthetic process, solar energy is converted into chemically accessible energy, carbohydrates and molecular  $O_2$ . [2, 3] Inspired by the natural photosynthesis process, much effort has been dedicated to using sunlight directly as the energy source for water splitting.[4] In such process, the water is oxidised to  $O_2$  [Eq.(1.1)], and then the electrons can be used to reduce protons to  $H_2$  [Eq.(1.2)], or reduce  $CO_2$  to methanol, methane, or other fuels.



When restricted to  $H_2$  and  $O_2$  evolution from water and sunlight, it falls into the category of light-driven water splitting.[5, 6] Usually the processes are accelerated by using expensive noble metals (such as platinum, ruthenium, iridium and rhodium) acting as water oxidation catalysts and hydrogen reduction catalysts.[7] However, these metals are not themselves sustainable resources, so the viability of water oxidation and hydrogen evolution relies on the design of novel, efficient and robust catalytic materials based on earth-abundant metals. Recently lots of attentions have been attracted to the design

of catalysts based on the first-row transition metals, including nickel, cobalt, iron, and manganese.[7, 8] However, none of the present catalysts satisfy the industrial requirements of stability, efficiency and speed. The properties of transition metal complexes involving in catalyst reaction process depends on the orbital interaction between metal and ligand orbitals. In order to design catalysts that have the potential capacities to fulfill the above requirements, better knowledge about the electronic structure as well as geometric information of transition metal complexes is required.

X-ray absorption spectra (XAS) is an essential method that can offer a unique probe of the local geometric and electronic structure of the element of interest. An electron can absorb a particular energy and then be excited to empty or partially filled orbitals just below the ionisation potential (IP) giving an edge, see Figure 1.1 which contains information about the unoccupied density of states. The energy of the absorption edge provides information about the oxidation and spin state of the absorbing atom. The choice of the energy of the X-ray used determines the specific element being probed.

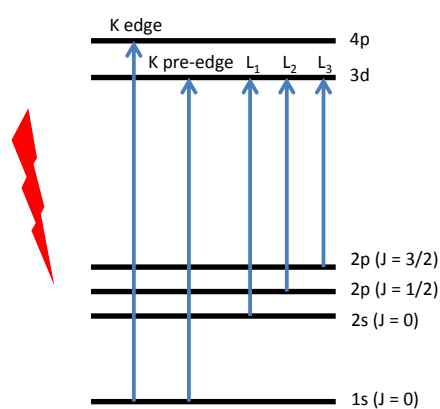


FIGURE 1.1: The energy level diagram for K edge transitions ( $1s \rightarrow 3d/4p$ ), and L-edge ( $L_1, L_2,$  and  $L_3$ ) transitions ( $2s/2p \rightarrow 3d$ ). The energy levels are not drawn to scale.

Modelling systems with well known structures have been very important to understand the XAS of catalysts and metallo-proteins.[9–13] As we are interested in 3d transition metals, the unoccupied and partially occupied metal valence 3d orbitals play an important role during the catalytic reactions. To probe the 3d orbital contribution to bonding, the metal L-edge ( $2p \rightarrow 3d$ ) XAS can be adopted to directly offer element-specific details of the metal 3d orbitals which are not observable in optical spectroscopy. Optical spectroscopy generally gives a picture of the total chemical bonding interactions, and not particular for the metal 3d orbitals, a limitation that also applies to other spectroscopy

techniques, e.g., electron paramagnetic resonance (EPR), magnetic circular dichroism (MCD), and resonance Raman (RR). For metal L-edge, a  $2p^5$  core hole is created after a formally electric dipole allowed  $2p \rightarrow 3d$  transition, which creates a characteristic absorption peak, see Figure 1.2. The  $2p^5$  core hole has a spin angular momentum  $S = 1/2$

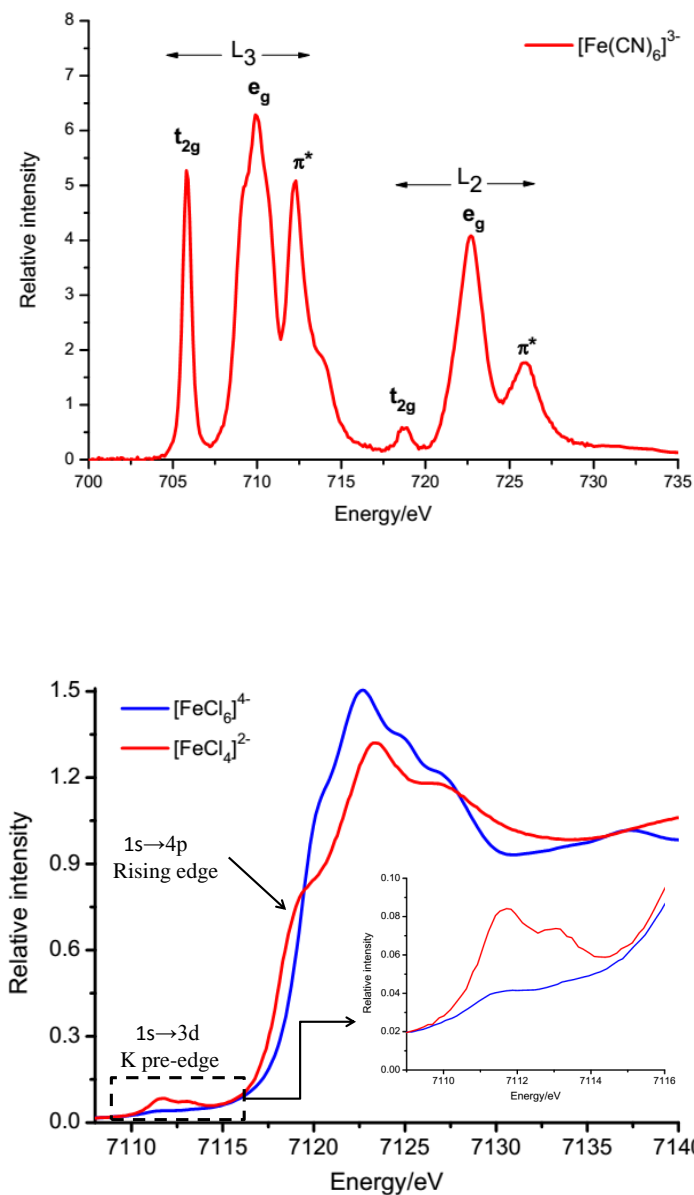


FIGURE 1.2: Upper: the experimental L-edge XAS of  $[\text{Fe}(\text{CN})_6]^{3-}$ . below: the K-edge XAS of centrosymmetric complex  $[\text{FeCl}_6]^{4-}$  and non-centrosymmetric complex  $[\text{FeCl}_4]^{2-}$ , the K pre-edge and rising edge are marked.

which can couple to the orbital angular momentum  $L = 1$  and produce  $J = 3/2$  and  $J = 1/2$  final states, see Figure 1.2. These final states ( $2p^5 3d^{n+1}$ ) are directly observable

in the L-edge spectrum as two main regions called  $L_3$  and  $L_2$  edge, see Figure 1.2. For the first-row transition metals (from scandium to copper), the energies of L-edges lie in the energy region from  $\sim 400$  to 1000 eV, which may have strong scattering by lighter elements (carbon, oxygen or nitrogen). Due to the limitations on the sample environment caused by the strong scattering, the soft L-edges XAS can not be directly used for transition metal catalysts in biological or solution systems .

To avoid these limitations in some applications like solar fuel system, we could alternatively use hard X-rays at K edge, which provides more freedom with respect to the sample environment. The main contribution to the K-edge spectrum is from  $1s \rightarrow np$  transitions, where  $np$  represents the unoccupied  $p$  orbitals of the targeting element, see Figure 1.2. For probing the  $3d$  orbital of transition metals, additional insights can be acquired by examining the features of the K pre-edge. Both the energy and intensity of the pre-edge features are highly sensitive to the metal  $3d$  orbitals, see Figure 1.2. The K pre-edge characters are usually associated with the electron transition from core  $1s$  orbital to unoccupied or partially occupied  $3d$ , and generate the  $1s^1 3d^{n+1}$  final states. The intensity of K pre-edge is largely increased when the centrosymmetric environment is broken (e.g., changing the coordination number) as distortions from centrosymmetry allow for  $4p$  character to delocalize into metal  $3d$  orbitals through their mutual interactions with the ligand orbitals. This  $3d-4p$  orbital hybridization is an important intensity mechanism as it gives rise to electric dipole-allowed transitions in the K pre-edge.[14] The admixture of  $3d$  and  $4p$  largely depends on the site symmetry, which could be easily interpreted using group point theory.[15] Usually the quadruple transition is  $\sim 2$  orders of magnitude weaker than a dipole transition. Que and co-workers showed that the iron K pre-edge intensity has a near linear correlation with the total amount of  $4p$  orbitals in the  $3d$ -type molecular orbitals.[16, 17] It is thus essential to be able to estimate the dipole contributions when a catalyst site changes during a reaction.

However, the metal K pre-edge features are not well resolved due to the short lifetime of the  $1s$  core hole, which gives a large natural bandwidth.[18] One possible solution is to use  $1s2p$  resonant inelastic X-ray scattering (RIXS), because the resolution in the energy transfer direction is determined only by the lifetime of the final state, not the lifetime of the  $1s$  core hole in the intermediate state.[19] The  $1s2p$  RIXS event can be thought of as a two-step process, The general energy scheme, taking iron as an example is presented in Figure 1.3. Starting from the initial state, one  $1s$  electron is excited into an unoccupied  $3d$  orbital via a quadruple transition, and subsequent electric dipole allowed decay of a  $2p$  electron into the  $1s$  hole, is detected by its photon emission. In a simplified picture the absorption process gives information of the empty electronic states, while the emission gives information about the occupied states. Thus, metal L-edge absorption and  $1s2p$  RIXS reach the same final state configurations, and allow a direct comparison but with

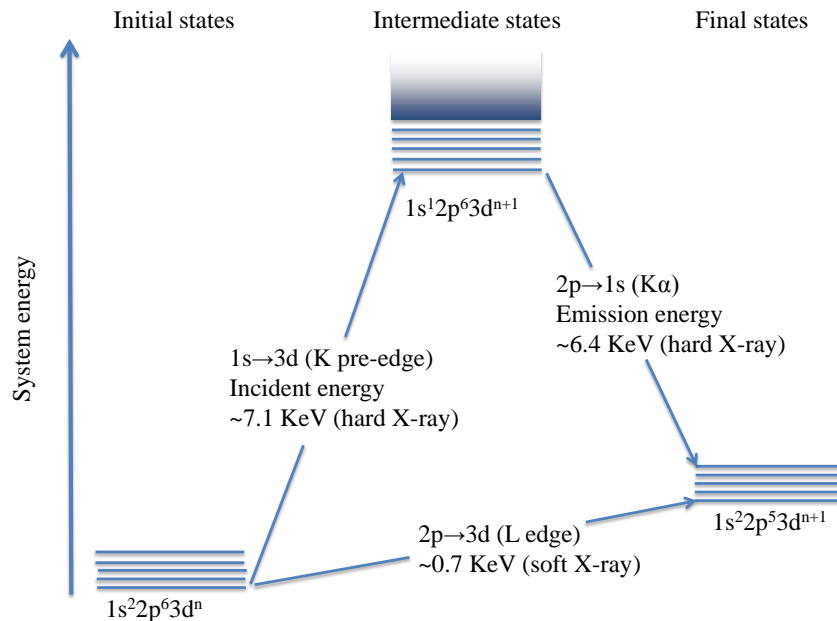


FIGURE 1.3: The Scheme for atomic iron  $1s2p$  RIXS, where a photon creates  $1s$  core hole excited states, then the  $1s$  core hole is filled by one  $2p$  electron and generating a  $2p$  core hole.

complementary selection rules. Recently, high-resolution RIXS spectra have been used to get detailed electronic structure information, *e.g.* the  $3d$  orbital covalency, using hard X-ray.[20–22] With RIXS experiments reaching 0.1 eV resolution in the energy transfer direction,[23] it becomes important to include both multiplet effects and charge-transfer states in the analysis.

Although the understanding of the X-ray spectra has matured, a detailed interpretation requires accurate simulations. X-ray spectra that involve core holes can be described by a number of different approaches, *e.g.* multiple scattering,[24, 25] transition-potential (TP) density-functional theory (DFT),[26] Bethe-Salpeter approach,[27, 28] and complex polarization propagator methods.[29] Recently, time dependent (TD) DFT method has been used to predict and interpret XAS.[30–33] This provides a framework to calculate transition energies and intensities with favourable balance between accuracy and computational time. A limitation of many of these approaches, is that they do not incorporate the necessary physics to correctly account for the multiplet effects arising from electron–electron correlations. A DFT restricted-open shell configuration interaction with singles (DFT/ROCIS) approach was developed to cover all the multiplets that arise from the atomic terms.[34–36] The limitation is that they are incapable of handling multiple excitations, which may restrict the descriptions of core hole induced

charge transfer (CT) features.

Another possibility to properly account for the multiplet effects is to use semi-empirical charge-transfer multiplet (CTM) model.[37, 38] This method includes all relevant final states and gives a balanced description of electron repulsion and spin-orbit coupling (SOC). It often achieves excellent agreement with experimental data for highly symmetric systems through a multi-parameter fit to the experimental spectrum.[39] However, the number of parameters used to describe the effects of the ligand environment increases with decreasing symmetry, which makes it difficult to describe complexes with low or no symmetry.

There is thus a need for a high-level method that can describe the electron correlation, SOC and charge transfer states of transition metal systems without fitting parameters. One such class of methods is the multi-configurational self consistent field (MCSCF) method.[40–42] Among these methods is the restricted active space self consistent field (RASSCF) method. In calculations, the most important orbitals are included in the active space, not only the metal character core and  $3d$  molecular orbitals (MOs), but also the important ligand MOs. The calculation can be further improved by including correlation with the occupied inactive and virtual orbitals using second order perturbation (RASPT2),[43–45] which is usually important for transition metal systems. The RAS method can be used to model X-ray processes by including also the core orbitals in the active space. As the number of excitations from the core orbitals can be restricted, usually to one, it is convenient to use the RAS.[46] The RAS method has been used to model soft XAS and RIXS spectra of several transition-metal systems.[47–54] The first applications of RAS on the K edge and  $1s2p$  RIXS are also tested.[55] The ratio between cost and accuracy can be optimized by a proper selection of active space, basis set and computational algorithms, and the method can potentially be applied to both small and medium-sized systems.[54]

## Chapter 2

# Computational framework

The recent experimental X-ray techniques progress can give subtle spectral features, which implying that the advanced quantum mechanism methods are required to accurately simulate and interpret the core level spectra, as outlined above. In this chapter, the important approximation and theory used to simulate the X-ray spectroscopies are introduced.

### 2.1 Born-Oppenheimer approximation

The nucleus has a much larger mass and much smaller velocity compared to the electron, assuming the motions of the nuclei can be ignored when describing the electrons in a molecule, and then the electron wave function depends upon the nuclei positions but not upon their velocities. This assumption is known as Born-Oppenheimer approximation,[56] which make it possible to simplify the complicated Schrödinger equation of a molecule. The nucleus and electron problems can be solved with independent wavefunctions from the separation of the nucleus and the electron motion.

The Schrödinger equation can be written as:

$$\hat{H}(\mathbf{r}, \mathbf{R})\Psi(\mathbf{r}, \mathbf{R}) = E(\mathbf{r}, \mathbf{R})\Psi(\mathbf{r}, \mathbf{R}) \quad (2.1)$$

The molecular wavefunction  $\Psi$  can be separated into a product of nuclear and electronic components:

$$\Psi(\mathbf{r}, \mathbf{R}) = \psi_n(\mathbf{R})\psi_e(\mathbf{r}, \mathbf{R}) \quad (2.2)$$

where  $\psi_n(\mathbf{R})$  is a wavefunction in terms of nuclear position,  $\psi_e(\mathbf{r}, \mathbf{R})$  is electronic wavefunction in terms of the positions of electron and nuclei. The quantity  $\mathbf{r}$  represents the coordinates of all electrons, and  $\mathbf{R}$  represents coordinates of all nuclei.

Going back to the Eq.(2.1), the total molecular Hamiltonian can be written as

$$\hat{H}(\mathbf{r}, \mathbf{R}) = \hat{H}_n(\mathbf{R}) + \hat{H}_e(\mathbf{r}, \mathbf{R}) \quad (2.3)$$

where

$$\hat{H}_n(\mathbf{R}) = \hat{T}_n + V_{nn}(\mathbf{R}) \quad (2.4)$$

$$\hat{H}_e(\mathbf{r}, \mathbf{R}) = \hat{T}_e + V_{ee}(\mathbf{r}) + V_{en}(\mathbf{r}, \mathbf{R}) \quad (2.5)$$

Here  $\hat{T}_n$  is kinetic energy operator of the nuclei,  $V_{nn}(\mathbf{R})$  is nuclei-nuclei repulsion Coulomb potential,  $\hat{T}_e$  is kinetic energy operator of the electron,  $V_{ee}(\mathbf{r})$  is electron-electron repulsion Coulomb potential, and  $V_{en}(\mathbf{r}, \mathbf{R})$  is electron-nuclei attraction Coulomb potential. Now substitute these terms and the Eq.(2.2) into the Schrödinger equation the Eq.(2.1), then obtain

$$(\hat{T}_n + V_{nn}(\mathbf{R}) + \hat{T}_e + V_{ee}(\mathbf{r}) + V_{en}(\mathbf{r}, \mathbf{R}))\Psi(\mathbf{r}, \mathbf{R}) = E(\mathbf{r}, \mathbf{R})\psi_n(\mathbf{R})\psi_e(\mathbf{r}, \mathbf{R}) \quad (2.6)$$

Consider the nuclei and electron kinetic energy operator acting on the wavefunction,  $\hat{T}_n$  contains derivatives in terms of nuclei coordinates, it has effects on both nuclei and electron wavefunction:

$$\hat{T}_n\psi_n(\mathbf{R})\psi_e(\mathbf{r}, \mathbf{R}) = \psi_n(\mathbf{R})\hat{T}_n\psi_e(\mathbf{r}, \mathbf{R}) + \psi_e(\mathbf{r}, \mathbf{R})\hat{T}_n\psi_n(\mathbf{R}) \quad (2.7)$$

Here, the  $\hat{T}_n\psi_e(\mathbf{r}, \mathbf{R})$  is much smaller than  $\hat{T}_n\psi_n(\mathbf{R})$ , hence the Eq(2.7) can be written as

$$\hat{T}_n\psi_n(\mathbf{R})\psi_e(\mathbf{r}, \mathbf{R}) \approx \psi_e(\mathbf{r}, \mathbf{R})\hat{T}_n\psi_n(\mathbf{R}) \quad (2.8)$$

$\hat{T}_e$  contains derivatives in terms of electron coordinates, and hence it only has effect on the electron wavefunction,

$$\hat{T}_e\psi_e(\mathbf{r}, \mathbf{R})\psi_n(\mathbf{R}) = \psi_n(\mathbf{R})\hat{T}_e\psi_e(\mathbf{r}, \mathbf{R}) \quad (2.9)$$

Apply the same fact in the the Schrödinger equation the Eq.(2.1), it can be written as

$$\psi_e(\mathbf{r}, \mathbf{R})\hat{H}_n(\mathbf{R})\psi_n(\mathbf{R}) + \psi_n(\mathbf{R})\hat{H}_e(\mathbf{r}, \mathbf{R})\psi_e(\mathbf{r}, \mathbf{R}) = E(\mathbf{r}, \mathbf{R})\psi_n(\mathbf{R})\psi_e(\mathbf{r}, \mathbf{R}) \quad (2.10)$$

Then divide the both sides of Eq. (2.10) by  $\psi_n(\mathbf{R})\psi_e(\mathbf{r}, \mathbf{R})$ , which gives

$$\frac{\hat{H}_e(\mathbf{r}, \mathbf{R})\psi_e(\mathbf{r}, \mathbf{R})}{\psi_e(\mathbf{r}, \mathbf{R})} = E - \frac{\hat{H}_n(\mathbf{R})\psi_n(\mathbf{R})}{\psi_n(\mathbf{R})} \quad (2.11)$$

The right side depends only on the coordinates of nuclei  $\mathbf{R}$ , and can be written compactly as function  $\varepsilon(\mathbf{R})$ . Substitute it in Eq(2.11) and obtain the electronic Schrödinger

equation:

$$\hat{H}_e(\mathbf{r}, \mathbf{R})\psi_e(\mathbf{r}, \mathbf{R}) = \varepsilon(\mathbf{R})\psi_e(\mathbf{r}, \mathbf{R}) \quad (2.12)$$

## 2.2 Hartree-Fock theory

The electronic Schrödinger equation was obtained from the Born-Oppenheimer approximation in section 2.1. The exact solution to the equation can only be reachable for one-electron systems, such as hydrogen atom or  $He^+$ . As long as one uses the electronic Schrödinger equation to deal with a many-body problem in quantum chemistry, only approximated solution can be obtained. Hartree-Fock theory is the simplest approximation method to solve many-body electronic Schrödinger equation.[57] It simplifies the N-electron problem into N one-electron problems. Hence, it is reasonable to start the wavefunction with a general form:

$$\Psi(\mathbf{r}_1, \mathbf{r}_2, \dots, \mathbf{r}_N) = \psi_1(\mathbf{r}_1)\psi_2(\mathbf{r}_2) \cdots \psi_N(\mathbf{r}_N) \quad (2.13)$$

when consider the full set of coordinates including space and spin, the Eq(2.13) can be rewritten as

$$\Psi(\mathbf{X}_1, \mathbf{X}_2, \dots, \mathbf{X}_N) = \chi_1(\mathbf{X}_1)\chi_2(\mathbf{X}_2) \cdots \chi_N(\mathbf{X}_N) \quad (2.14)$$

Clearly, this wavefunction can not satisfy the Pauli principle, which the wavefunction has to be antisymmetric. In order to fulfil the antisymmetric requirement, the wavefunction of the simplest two-electron many-body system can be written like below:

$$\Psi(\mathbf{X}_1, \mathbf{X}_2) = \frac{1}{\sqrt{2}}[\chi_1(\mathbf{X}_1)\chi_2(\mathbf{X}_2) - \chi_1(\mathbf{X}_2)\chi_2(\mathbf{X}_1)] \quad (2.15)$$

The wavefunction also can be represented using determinants like

$$\Psi(\mathbf{X}_1, \mathbf{X}_2) = \frac{1}{\sqrt{2}} \begin{vmatrix} \chi_1(\mathbf{X}_1) & \chi_2(\mathbf{X}_1) \\ \chi_1(\mathbf{X}_2) & \chi_2(\mathbf{X}_2) \end{vmatrix} \quad (2.16)$$

Now it is easy to expand the determinant for N-electron system

$$\Psi(\mathbf{X}_1, \mathbf{X}_2, \dots, \mathbf{X}_N) = \frac{1}{\sqrt{2}} \begin{vmatrix} \chi_1(\mathbf{X}_1) & \chi_2(\mathbf{X}_1) & \cdots & \chi_N(\mathbf{X}_1) \\ \chi_1(\mathbf{X}_2) & \chi_2(\mathbf{X}_2) & \cdots & \chi_N(\mathbf{X}_2) \\ \vdots & \vdots & \vdots & \vdots \\ \chi_1(\mathbf{X}_N) & \chi_2(\mathbf{X}_N) & \cdots & \chi_N(\mathbf{X}_N) \end{vmatrix} \quad (2.17)$$

The electronic Hamiltonian can be written in a simple way as

$$\hat{H}_e = \sum_i \zeta(\alpha) + \sum_{\alpha < \beta} \eta(\alpha, \beta) + V_{nn}(\mathbf{R}) \quad (2.18)$$

where  $\zeta(\alpha)$  represents a one-electron operator,  $\eta(\alpha, \beta)$  represents a two-electron operator, and  $V_{nn}(\mathbf{R})$  is a constant for the fixed set of nuclei coordinates  $\mathbf{R}$ . Similarly, the electronic energy in terms of integrals can also be expressed using one-electron and two-electron operators:

$$E = \sum_{\alpha} \langle \alpha | \zeta | \alpha \rangle + \frac{1}{2} \sum_{\alpha\beta} ([\alpha\alpha|\beta\beta] - [\alpha\beta|\beta\alpha]) \quad (2.19)$$

where  $\langle \alpha | \zeta | \alpha \rangle$  is one-electron integral,  $[\alpha\alpha|\beta\beta]$  is two-electron Coulomb integral,  $[\alpha\beta|\beta\alpha]$  is exchange integral, these integrals can be easily computed by existing efficient computer algorithms. Under HF approximation, the electron feels only the average potential of the other electrons, which means there is no explicit electron correlation energy other than that of parallel-spin electrons, introduced by the exchange term. The energy difference between the exact solution of the non-relativistic Schrödinger equation and the solution of HF equation using a complete basis is called correlation energy. The electron correlation can be separated into two components namely static correlation and dynamical correlation.[58]

## 2.3 Multi-configurational method

The static correlation can be well described by multi-configurational self consistent field (MCSCF) methods, among which the most widely adopted approaches is complete active space SCF (CASSCF).[40] The MCSCF wavefunction can be written in a configuration interaction (CI) form as:

$$\Psi_{MCSCF} = \sum_M C_M \Phi_M \quad (2.20)$$

where  $\phi_M$  are Slater determinant or configuration state functions, which can be selected as all possible ones formed within a given active space. For the 3d transition metal complexes, there are lots of electronic configurations with very similar energies and the mixing among these configurations are very strong. In such cases, multi-configurational based method is required to describe the electronic structure. To describe this strong correlation, one have to incorporate these important configurations in the reference space. The CASSCF method accounts for the most important configurations by introducing a set of orbitals, and then all possible configurations within the active space are produced.

The orbitals included in the active space are called active orbitals, and they can be doubly occupied, singly occupied or empty. These orbitals are optimized through all possible rotations between the active orbitals and inactive orbitals, active orbitals and secondary orbitals, inactive orbitals and secondary orbitals. The computation of CASSCF becomes demanding with the increase of the number of active orbitals, especially when the number of active orbitals is close to the number of electrons. To reduce the computational cost, the active space can be partitioned into subspaces, namely a restricted active space SCF (RASSCF) method.[46] In this method, the excitation level is usually limited to one or two electrons, hence give a limited number of excited configurations.

### 2.3.1 Second-order perturbation

The CAASCF/RASSCF method can describe correlation well within the chosen reference space, however, remaining correlation calling dynamic correlation is still neglected. The dynamical correlation can be treated perturbatively using CASPT2,[59] which uses a CASSCF reference wavefunction. The Eq(2.1) is a unperturbed equation, and we can solve it in a parameterized form. The Hamiltonian can be written as:

$$\hat{H}(\mathbf{r}, \mathbf{R}) = \hat{H}_0(\mathbf{r}, \mathbf{R}) + \gamma \hat{H}_1(\mathbf{r}, \mathbf{R}) + \gamma^2 \hat{H}_2(\mathbf{r}, \mathbf{R}) + \dots \quad (2.21)$$

the wavefunction can be written as:

$$\Psi(\mathbf{r}, \mathbf{R}) = \Psi_0(\mathbf{r}, \mathbf{R}) + \gamma \Psi_1(\mathbf{r}, \mathbf{R}) + \gamma^2 \Psi_2(\mathbf{r}, \mathbf{R}) + \dots \quad (2.22)$$

and the energy can be written as:

$$E(\mathbf{r}, \mathbf{R}) = E_0(\mathbf{r}, \mathbf{R}) + \gamma E_1(\mathbf{r}, \mathbf{R}) + \gamma^2 E_2(\mathbf{r}, \mathbf{R}) + \dots \quad (2.23)$$

The chain equation can be obtained as the solution is independent on the  $\gamma$ :

$$\hat{H}_0(\mathbf{r}, \mathbf{R})\Psi_0(\mathbf{r}, \mathbf{R}) = E_0(\mathbf{r}, \mathbf{R})\Psi_0(\mathbf{r}, \mathbf{R}) \quad (2.24)$$

$$(\hat{H}_0(\mathbf{r}, \mathbf{R}) - E_0(\mathbf{r}, \mathbf{R}))\Psi_1(\mathbf{r}, \mathbf{R}) = (E_1(\mathbf{r}, \mathbf{R}) - \hat{H}_1(\mathbf{r}, \mathbf{R}))\Psi_0(\mathbf{r}, \mathbf{R}) \quad (2.25)$$

$$(\hat{H}_1(\mathbf{r}, \mathbf{R}) - E_1(\mathbf{r}, \mathbf{R}))\Psi_2(\mathbf{r}, \mathbf{R}) = (E_2(\mathbf{r}, \mathbf{R}) - \hat{H}_2(\mathbf{r}, \mathbf{R}))\Psi_1(\mathbf{r}, \mathbf{R}) \quad (2.26)$$

From Eq. (2.25), the first order waverfunction can be written as a linear combination of zero-order functions:

$$\Psi_1(\mathbf{r}, \mathbf{R}) = \sum_n c_n \Psi_{0,n}(\mathbf{r}, \mathbf{R}) \quad (2.27)$$



the important valence orbitals are included in RAS2, where all possible excitations are allowed. The core orbitals ( $1s$  or  $2p$ ) are included in RAS1 allowing a maximum of one hole, or in RAS3, with single and double excitation allowed. Orbital optimization has been performed separately for ground and excited states. For the calculations of the core excited states, the weights of all configurations with doubly occupied core orbitals have been set to zero. To avoid orbital rotation, the core orbitals have been frozen in the orbital optimization of the final states. In a second step, dynamical correlation is included using second-order perturbation (RASPT2).[43–45]

Scalar relativistic effects have been included by using a Douglas-Kroll Hamiltonian[61] in combination with a relativistic atomic natural orbital basis set ANO-RCC-VTZP.[62, 63] To speed-up calculations without sacrificing accuracy, the density-fitting approximation of the electron repulsion integrals has been used, using auxiliary basis sets from an atomic-compact Cholesky decomposition.[64, 65]

SOC is calculated from a one-electron spin-orbit Hamiltonian based on atomic mean field integrals.[60, 66] The SOC free eigenstates are used as a basis for computing SOC matrix elements, and the spin-orbit eigenstates are then obtained by diagonalizing the SOC matrix, giving SOC states  $|\xi\rangle$ , which are linear combinations of SOC free states  $|\eta\rangle$ :

$$|\xi\rangle = \sum_{\eta} c_{\eta}^{\xi} |\eta\rangle \quad (2.29)$$

The weight ( $\omega$ ) from each SOC free state can be acquired from the square of the coefficient  $(c_{\eta}^{\xi})^2$ . These eigenstates are then utilized to calculate the strength of the transitions using the restricted active space state interaction (RASSI) approach. The corresponding equation for the 1st order cartesian multipole moments (dipole transition moment operator,  $\vec{\mu}_{\sigma\delta}$ ) is:

$$f_{(\sigma\rightarrow\delta)}^D = \frac{2m_e}{3\hbar^2 e^2} \Delta E_{\sigma\delta} |\vec{\mu}_{\sigma\delta}|^2 \quad (2.30)$$

The quadrupole transition intensity ( $f_{(\sigma\rightarrow\delta)}^Q$ ) of the  $1s$  to  $3d$  transition, is consist of electric quadrupole electric quadrupole contribution  $f^{qq}$ , magnetic dipole magnetic dipole contribution  $f^{mm}$ , the electric quadrupole magnetic dipole contribution  $f^{qm}$ , electric dipole electric octupole contribution  $f^{\mu o}$ , and electric dipole magnetic quadrupole contribution  $f^{\mu\varpi}$ . [67]

$$f_{(\sigma\rightarrow\delta)}^Q = \frac{m_e}{20\hbar^4 e^2 c^2} \Delta E_{\sigma\delta}^3 [ |\vec{T}_{\sigma\delta}^q|^2 + |\vec{T}_{\sigma\delta}^m|^2 + 2Re(T_{\sigma\delta}^{q,*} T_{\sigma\delta}^m) + 2Re(T_{\sigma\delta}^{\mu,*} T_{\sigma\delta}^o) + 2Re(T_{\sigma\delta}^{\mu,*} T_{\sigma\delta}^m) ] \quad (2.31)$$

it can be simplified as

$$f_{(\sigma\rightarrow\delta)}^Q = f_{(\sigma\rightarrow\delta)}^{qq} + f_{(\sigma\rightarrow\delta)}^{mm} + f_{(\sigma\rightarrow\delta)}^{qm} + f_{(\sigma\rightarrow\delta)}^{\mu o} + f_{(\sigma\rightarrow\delta)}^{\mu\varpi} \quad (2.32)$$

where  $m_e$  and  $e$  are the mass and charge of the electron, respectively,  $\hbar$  is reduced Planck constant,  $c$  is the speed of light in atomic units,  $\Delta E_{\sigma\delta}$  is the transition energy, and  $T$  is transition moment. The quadrupole transition intensities were calculated with a locally developed RASSI module. Vibronic effects have small effects on the K pre-edge features of these systems and have been neglected. The RIXS calculation is theoretically described by the Kramers-Heisenberg formula[68]:

$$F(\Omega, \omega) = \sum_f \left| \sum_n \frac{\langle f|T_e|i\rangle \langle i|T_a|g\rangle}{K(\Gamma_i)} \right|^2 \times K(\Gamma_f) \quad (2.33)$$

where the scattering intensity  $F$  is a function of incident energy ( $\Omega$ ) and emitted X-ray energy ( $\omega$ ), the  $|g\rangle$ ,  $|i\rangle$ , and  $|f\rangle$  are ground, intermediate and final states respectively.  $T_a$  and  $T_e$  are transition operators for the absorption and emission processes respectively.  $K(\Gamma)$  depends on the resonance energy and the lifetime broadening  $\Gamma$  of each state.

### 2.3.3 Orbital contribution analysis

A chemically intuitive molecular orbital picture have been used to analyze the X-ray spectroscopy.[52] The orbital contribution analysis is based on the changes in orbital occupation numbers during a excitation multiplying the intensity of that particular excitation. In metal L-edge and K pre-edge calculations, the numbers of natural occupation numbers the active orbitals are available for each RASSCF state, and can be constructed for multi-state (MS)-RASPT2 and RASSI SOC states as they are just linear combinations of RASSCF states. The differences in occupation numbers between the ground state and each final state allows for an intuitive interpretation of the spectrum in terms of orbital excitations. The orbital contribution of orbital  $i$  involved in a particular transition can be expressed as:

$$f_{(\sigma \rightarrow \delta)}^i = \frac{\sum_{\alpha} \omega_{\alpha}^{\sigma} \sum_{\beta} \omega_{\beta}^{\delta} f_{(\alpha \rightarrow \beta)} (n_{\beta}^i - n_{\alpha}^i)}{\sum_{\alpha} \omega_{\alpha}^{\sigma} \sum_{\beta} \omega_{\beta}^{\delta} f_{(\alpha \rightarrow \beta)}} f_{(\sigma \rightarrow \delta)}^{\Delta} \quad (2.34)$$

where  $\omega$  is the weight of the SOC free state in the SOC state,  $n_{\alpha}^i$  and  $n_{\beta}^i$  represents the natural occupation number of orbital  $i$  in  $\alpha$  and  $\beta$  SOC free state respectively,  $f_{(\alpha \rightarrow \beta)}$  is the transition intensity between  $\alpha$  and  $\beta$  SOC free state, and  $f_{(\sigma \rightarrow \delta)}^{\Delta}$  represents either dipole transition intensity in L-edge calculation or quadrupole transition intensity in K pre-edge calculation.

## 2.4 Charge transfer multiplet model

To properly account for the multiplet effects, a possibility is to use the semi-empirical charge transfer multiplet (CTM) model.[38] This method includes all relevant final states and gives a balanced description of electron-electron interactions and SOC with the ligand-field splitting introduced as parameters. For a free atom without any influence from the surroundings, the Hamiltonian for an N-electron atom can be written as:

$$H = \sum_N \frac{P_i^2}{2m} + \sum_N \frac{-Ze^2}{r_i} + \sum_N \vartheta(r_i) l_i \cdot s_i + \sum_{pairs} \frac{e^2}{r_{ij}} \quad (2.35)$$

where the first term denotes the kinetic energy of electrons, the second term denotes the electrostatic interaction of electrons with the nucleus, the third term denotes the SOC, and the last term denotes electron-electron repulsion. In a given configuration, the first two terms in the Hamiltonian represent the average energy of the configuration and have no contribution to the multiplet splitting. The last two terms represent the relative energy of the different terms within configurations and have contribution to the multiplet splitting. The ligand field is treated as a perturbation to the free atomic case and is introduced by adding a new term in the atomic Hamiltonian. For the highly covalent molecular systems, the charge transfer features are included by configuration interactions between the ground state ( $d^n$ ) and introduced extra LMCT (LMCT configuration ( $d^{n+1}\underline{L}$ ), and MLCT configurations states (additional MLCT configuration  $d^{n-1}L^-$ ). The CTM model often achieves excellent agreement with experimental data for highly symmetric systems through a multi-parameter fit to the experimental spectrum. However, the number of parameters used to describe the effects of the ligand environment increases with decreasing symmetry, which makes it difficult to describe complexes with low or no symmetry. Moreover, when both dipole and quadrupole transitions have to be accounted for, additional parameters describing the amount of mixing are required. This makes it less straightforward to apply and analyze the results of the CTM method for low-symmetry complexes.



## Chapter 3

# Simulation of the metal L-edge XAS

In this chapter, selected results from the RAS simulations of L-edge XAS are presented. It has been proved that the RAS can handle a number of different interactions: electron-electron interaction, SOC, and charge transfer between metal and ligands.[47, 51, 52, 54, 69] The high accuracy of the RAS results make them useful in fingerprinting the electronic structures of molecular systems without any prior knowledge. The RAS method is firstly used to simulate the atomic  $Fe^{3+}$  with charges, then it is extended to calculate the metal L-edge XAS of  $[Fe(CN)_6]^{3-}$  complex. The active orbital diagram is presented in Figure 3.1.

### 3.1 Atomic calculation of $Fe^{3+}$

The RAS and semi-empirical CTM model L-edge XAS of the  $Fe^{3+}$  ion a strong field are displayed in Figure 3.2. Ferric systems with a strong field have a low-spin  ${}^2T_{2g}(t_{2g})^5(e_g)^0$  ground state. The calculation is completed with active space RASPT2(11,1,0;3,5,0) using the ANO-RCC...3s2p1d basis set. The RAS spectra overlap well with the CTM model results. To understand the role of SOC from  $2p$  or  $3d$  orbitals and the multiplet effects on the L-edge spectral features, the spectrum of low-spin  $Fe^{3+}$  ion was analysed in detail, see Figure 3.3. Without SOC, there is only one edge, split by ligand field and multiplet effects. The spectrum is split into into  $L_3$  ( $J = \frac{3}{2}$ ) and  $L_2$  ( $J = \frac{1}{2}$ ) edges by including  $2p$  SOC, and the mixing of states with different multiplicity can further change the spectral features.

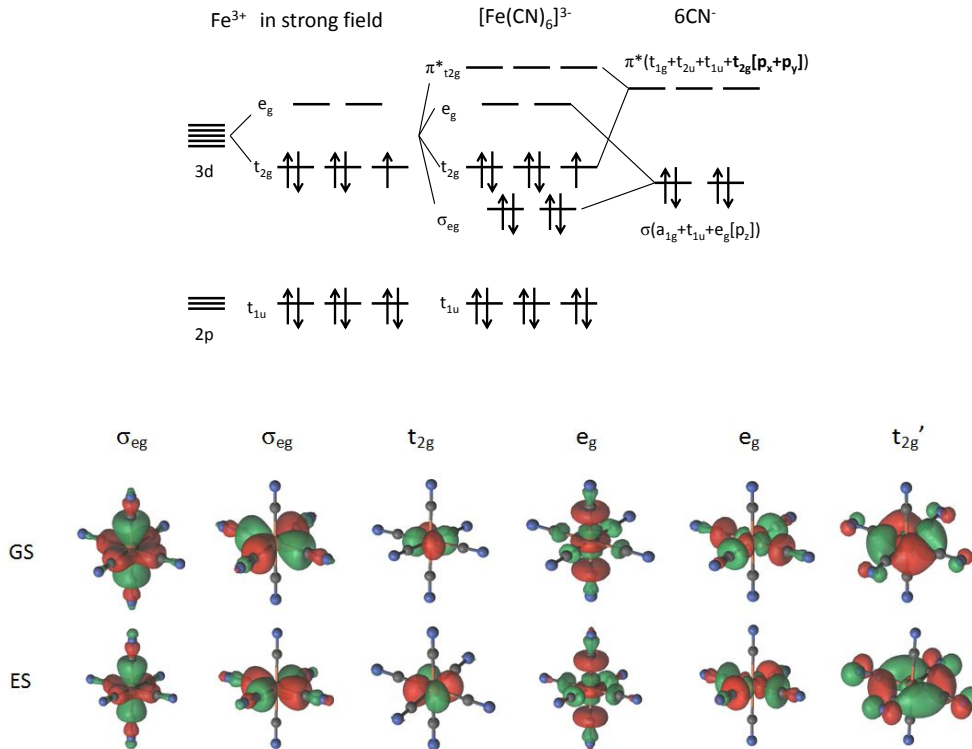


FIGURE 3.1: Schematic molecular orbital diagrams for low-spin  $Fe^{3+}$  and  $[Fe(CN)_6]^{3-}$ . The selected active orbitals for  $[Fe(CN)_6]^{3-}$  in ground and excited state are presented below.

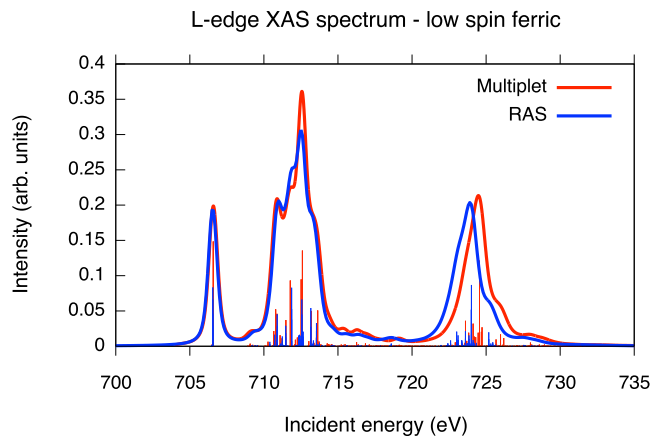


FIGURE 3.2: L-edge XAS spectra of the  $Fe^{3+}$  ion, with strong ligand-field splitting using RAS (blue) and the CTM model (red).

The  $3d$  SOC constant (0.05 eV) is much weaker compared to the  $2p$  one (8 eV), but still has important effects on the spectra. Without  $3d$  SOC, the ground state is six-fold degenerate stems from a three-fold orbital degeneracy and a doublet spin multiplicity.  $3d$  SOC splits these six states into doubly-degenerate  $J=\frac{1}{2}$ ,  $\Gamma_7^+$  in Bethe double-group notation, and four-fold degenerate  $\Gamma_8^+$  ( $J = \frac{3}{2}$ ) states, with the  $\Gamma_7^+$  states lower in energy

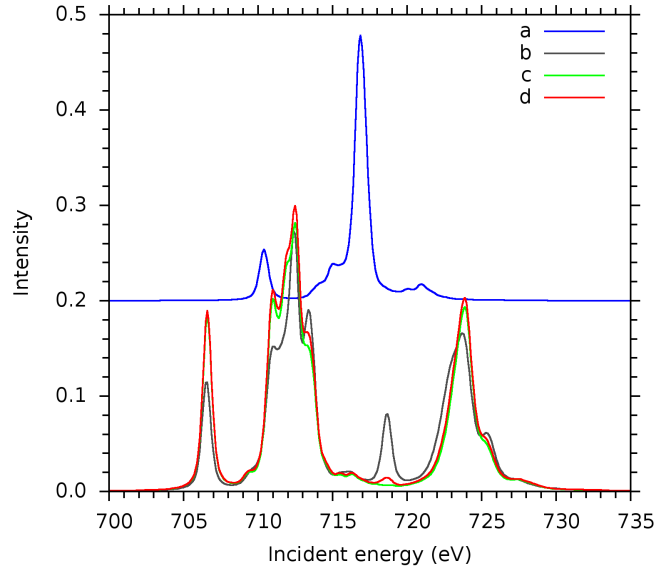


FIGURE 3.3: RAS L-edge XAS spectra of the  $Fe^{3+}$  ion with different treatments of  $2p$  and  $3d$  SOC. (a) Spectrum calculated without SOC. (b) Spectrum with  $2p$  SOC but using one of the  ${}^2T_{2g}$  ground states, i.e., without considering splitting from  $3d$  SOC. (c) Spectrum calculated from the  $\Gamma_7^+$  ( $J=\frac{1}{2}$ )  $3d$  SOC ground states. (d) Spectrum calculated from a Boltzmann distribution of  $\Gamma_7^+$  ( $J=\frac{1}{2}$ ) and  $\Gamma_8^+$  ( $J=\frac{3}{2}$ ) states.

by 0.086 eV, see Figure 3.4. The changes in spectral shape are connected to differences

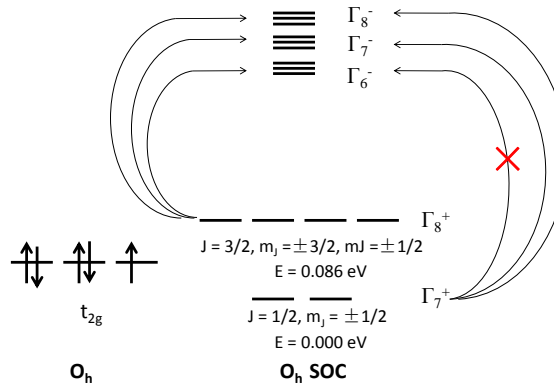


FIGURE 3.4: Energy levels of the SOC ground states with configuration  ${}^2T_{2g} 2p^6(t_{2g})^5(e_g)^0$  for the low-spin  $Fe^{3+}$  ion. The selection rule of transition is indicated with arrows, the forbidden transition from  $\Gamma_7^+$  ground state to  $\Gamma_6^-$  excited state is marked with a cross.

in selection rules for the different SOC states where e.g., transitions to the  $L_2 t_{2g}$  peak ( $\Gamma_6^-$ ) are electric dipole forbidden.  $3d$  SOC also leads to changes in the broad  $2p \rightarrow e_g$  resonance, partly because there are  $\Gamma_6^-$  states also in this region, and partly because the change in ground state leads to differences in the intensity mechanisms.[21] This example shows how a correct description of the multi-reference character of the degenerate ground

state, together with an accurate description of  $3d$  SOC, is required for the modeling of L-edge XAS spectra. A further improvement is to allow for a Boltzmann population of the different initial states. However, with a splitting of 0.086 eV only a minor fraction (3.5%) populates the  $\Gamma_8^+$  states at room temperature and the effect on the calculated specrossctrum is relatively small, see Figure 3.3. The intensities of transitions arising from  $\Gamma_8^+$  state will significantly depend on the temperature, since the state will be more populated at higher temperature.

### 3.2 Metal L-edges of low spin $[Fe(CN)_6]^{3-}$

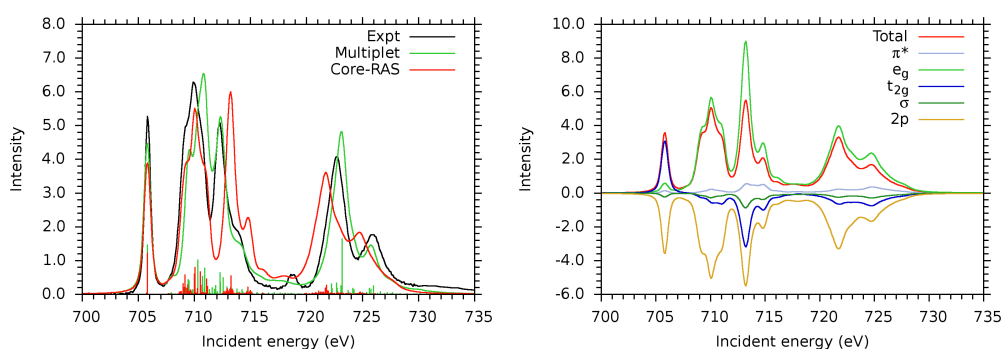


FIGURE 3.5: Metal L-edge of low spin  $[Fe(CN)_6]^{3-}$  (black: experiment, green: multiplet, red: RAS) and the corresponding orbital contribution analysis to the RAS calculated spectrum.

The experimental L-edge XAS spectrum of  $[Fe(CN)_6]^{3-}$  has three distinct peaks at the  $L_3$  edge, located at 705.8 eV, 710 eV and 712 eV respectively. There are two peaks in the  $L_2$  edge, the main peak at 722.8 eV and a minor peak at 726 eV.[70] The RAS calculation included two ligand-dominated filled  $\sigma$  orbitals, three empty ligand-centered antibonding ( $\pi^*$ ) orbitals and five metal  $3d$  character orbitals, giving RASPT2(15,1,0;3,10,0) active space, see Figure 3.1. The RAS calculation captures all the important spectral features of the experimental spectrum, see Figure 3.5. The RAS calculation overestimated the intensity of the third peak at the  $L_3$  edge, and the energy of that peak was also overestimated by  $\sim 1.5$  eV. While the energy of  $L_2$  edge was underestimated by  $\sim 1.0$  eV. This is due to an error in the calculation of the strength of the  $2p$  SOC. The accuracy of the RAS spectrum is comparable to that achieved with the semi-empirical CTM model.

Through the molecular orbital contributions to the  $[Fe(CN)_6]^{3-}$  L-edge XAS, see Figure 3.5, the first peak at 705.8 eV can be assigned to a  $2p \rightarrow t_{2g}$  transition. The second peak at 710 eV is mainly from  $2p \rightarrow e_g$  excitations. The third peak at around 713.2 eV is from  $2p \rightarrow \pi^*$  transitions together with  $t_{2g} \rightarrow e_g$  excitations. There are also large

---

changes in the occupation number of the  $t_{2g}$  orbitals, which reflects the increased weight of configurations with less than five  $t_{2g}$  electrons at this energy. The contributions for  $L_2$  edge are mainly from the  $2p \rightarrow e_g$  excitations, with very small  $2p \rightarrow \pi^*$  transitions.



## Chapter 4

# Simulation of the metal K pre-edge XAS

The intensities and relative energies of metal K pre-edge features have high sensitivities to both geometric and electronic structure. It can be used to probe dilute enzymatic systems and working catalysts.[9, 13] With the emergence of RIXS that can give high-resolution spectral information, it has become important to find theoretical method that accurately simulate and interpret spectroscopy in the K edge. It requires a method can treat the different important effects that shape the spectral features: ligand-field splitting, multiplet structures,  $3d-4p$  orbital hybridization, and charge-transfer transitions. Here the RAS method is introduced for the first time to calculate metal K pre-edge spectra of open-shell transition metal systems. The performance of RAS method is tested by applying it to six iron complexes;  $[FeCl_6]^{n-}$ ,  $[FeCl_4]^{n-}$ , and  $[Fe(CN)_6]^{n-}$  in ferrous and ferric oxidation states. The RAS calculations reproduces the spectral shape of all complexes with an average error for the peak splitting of only 0.1 eV, see Table 4.1.[55] The accuracy with which both intensities and relative energies can be well reproduced, suggests that the RAS method can be used to identify and predict changes in metal K pre-edge spectra that comes from changes in both oxidation state and ligand environment. The results for complexes  $[FeCl_6]^{4-}$ ,  $[FeCl_4]^{2-}$ , and  $[Fe(CN)_6]^{3-}$  will be mainly discussed in this thesis.

### 4.1 Multiplet structure

The  $[FeCl_6]^{4-}$  complex has  $\sigma$  and  $\pi$  donor ligands. The  $[FeCl_6]^{4-}$  experimental spectrum appears to have two pre-edge peaks, but a closer analysis reveals two close-lying

TABLE 4.1: Energies (in eV) and fitted pre-edge areas from experiment and theory.

	Experiment <sup>a</sup>	RAS	CTM <sup>d</sup>	TD-DFT <sup>e</sup>
<i>[FeCl<sub>6</sub>]<sup>3-</sup></i>				
E1(int)	7112.8(2.6)	-	-	-
E2(int)	7114.0(1.4)	7114.1	7114.0	7113.6
E3(int)	-	7118.3	7118.7	-
ratio <sup>b</sup>	3.7:2.0	3.5:2.0:0.7	3.4:2.0:0.4	-
<i>[FeCl<sub>6</sub>]<sup>4-</sup></i>				
E1(int)	7111.3(1.2)	-	-	-
E2(int)	7111.8(1.8)	7111.9	7112.1	7112.3
E3(int)	7113.4(0.6)	7113.4	7113.5	-
ratio <sup>b</sup>	2.0:3.0:1.0	1.8:0.9:1.0	1.8:1.0:1.0	-
<i>[FeCl<sub>4</sub>]<sup>1-</sup></i>				
E1(int)	7113.2(20.7)	-	-	7113.2
E2(int)	-	7116.6	-	-
<i>D/Q</i> ratio <sup>c</sup>	3.2:1.0	3.5:1.0	-	7.0:1.0
<i>[FeCl<sub>4</sub>]<sup>2-</sup></i>				
E1(int)	7111.6(8.6)	-	-	-
E2(int)	7113.1(4.3)	7113.1	-	7112.3
<i>D/Q</i> ratio <sup>c</sup>	2.3:1.0	2.4:1.0	-	7.5:1.0
<i>[Fe(CN)<sub>6</sub>]<sup>4-</sup></i>				
E1(int)	7112.9(4.2)	-	-	-
E2(int)	-	7115.6	7115.1	7113.5
ratio <sup>b</sup>	-	2.0:1.0	4.0:1.0	-
<i>[Fe(CN)<sub>6</sub>]<sup>3-</sup></i>				
E1(int)	7110.1(1.0)	-	-	-
E2(int)	7113.3(4.1)	7113.3	7113.4	7113.6
E3(int)	-	7117.3	7117.1	7115.2
ratio <sup>b</sup>	1.0:4.1	1.0:4.2:1.6	1.0:4.4:0.2	-

<sup>a</sup> Energies and fitted pre-edge areas (x100) from reference [39].

<sup>b</sup> Intensity ratio between peaks.

<sup>c</sup> Ratio between electric dipole (*D*) and electric quadrupole (*Q*) contributions.

<sup>d</sup> CTM results.

<sup>e</sup> TD-DFT results (BP86 functional) from reference [30].

states (at 7111.3 and 7111.8 eV), followed by a third state at higher energy (7113.4 eV), see Figure 4.1 and Table 4.1.

For *[FeCl<sub>6</sub>]<sup>4-</sup>*, the ground state has an electronic configuration  $t_{2g}^4 e_g^2$ . After electron excitation from *1s* to metal *3d* character orbitals, the excited configuration  $t_{2g}^5 e_g^2$  can only give a  $^4T_{1g}$  symmetry state. The excited configuration  $t_{2g}^4 e_g^3$  gives rise to  $^4T_{1g}$  and  $^4T_{2g}$  terms, which are split by *3d*–*3d* electron interactions, see Figure 4.1. The difference between the two  $e_g$  final states is most easily seen by considering a wavefunction where the spin-down  $t_{2g}$  electron is in the  $d_{xy}$  orbitals. In that case the  $^4T_{2g}$  state has the spin-down  $e_g$  electron in the  $d_{z^2}$  orbital, while in the  $^4T_{1g}$  state it is in the  $d_{x^2-y^2}$  orbital, see Figure 4.2. In the latter case, the two orbitals are in the same plane, leading to a larger electron-electron repulsion than if the orbitals are in different planes. The energy difference can be used as an indirect measure of orbital covalency, because higher covalency decreases the d-d repulsion, and thus the energy difference between the two

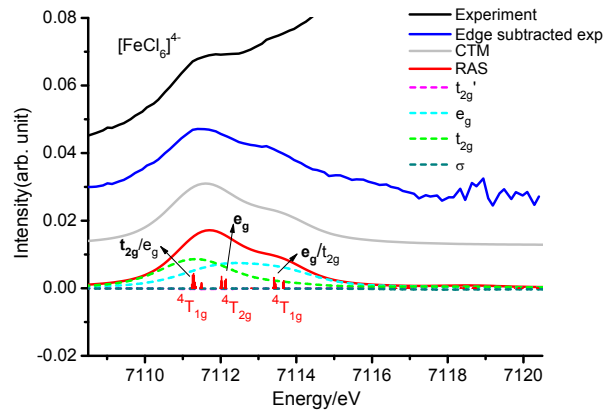


FIGURE 4.1: K pre-edge XAS of  $[FeCl_6]^{4-}$ . Experimental spectra (black), the edge-subtracted spectra (blue), CTM calculation spectra (light gray), RAS calculations spectra (red). The orbital contribution analyses are shown using dash lines, the main contributions are marked in bold. Contributions from 1s orbital are omitted.

$e_g$  states. However, this energy difference does not provide information about individual covalencies, only the combined effect of both  $e_g$  and  $t_{2g}$ .

The two  ${}^4T_{1g}$  states can mix because they belong to the same irreducible representations, this is visible in the orbital contribution analysis where the two peaks include contributions from both  $t_{2g}$  and  $e_g$  orbitals, see Figure 4.1. The experimental splitting between the first  ${}^4T_{1g}$  state and the  ${}^4T_{2g}$  state is around 0.5 eV, the between the two  ${}^4T_{1g}$  states, it is 2.1 eV.[39] The splittings are around 0.6 eV and 2.1 eV in the RAS calculations. These three states form two main peaks with separation of  $\sim 2.0$  eV in the RAS calculation, which overlaps very well with the experimental value of  $\sim 2.1$  eV.[39] The separation for  $[FeCl_6]^{4-}$  originates from not only ligand field effects, but also electron-electron interactions. The CTM calculation gave a separation energy of  $\sim 1.9$  eV. A DFT calculation with the BP86 functional gave  $\sim 1.0$  eV separation energy.[30]

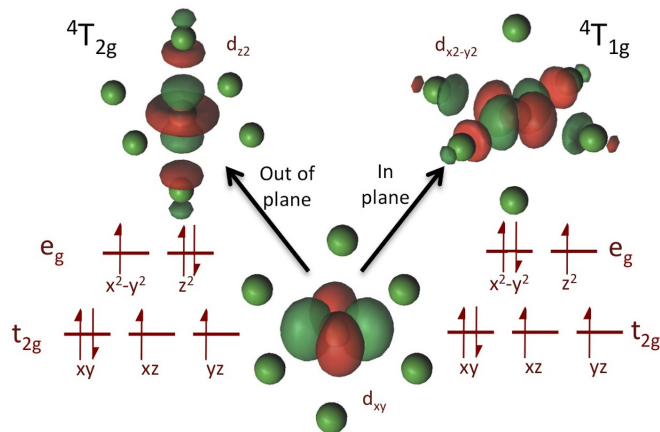


FIGURE 4.2: Difference in occupation between  ${}^4T_{2g}$  and  ${}^4T_{1g}$  valence states after  $1s \rightarrow 3d(e_g)$  excitation of a high-spin  $d^6$  system.

## 4.2 Hybridization of dipole and quadrupole contributions

As we mentioned in the beginning, breaking the centrosymmetry will give rise to dipole transitions to the hybridized orbitals, which largely increase the K pre-edge intensity.[14, 39] We here take  $[FeCl_4]^{2-}$  as a typical instance to disentangle the dipole and quadrupole contributions when the symmetry distorts from centrosymmetric  $O_h$  to noncentrosymmetric  $T_d$ . Comparing the experimental K pre-edge spectra, we could see that the total intensity for  $T_d$  symmetry  $[FeCl_4]^{2-}$  is largely increased. The ratio of total intensity between  $[FeCl_4]^{2-}$  and  $[FeCl_6]^{4-}$  is  $\sim 3.6:1$ . The dipole and quadrupole contribution ratio is  $\sim 2.3:1$  for  $[FeCl_4]^{2-}$ , see Table 4.1.

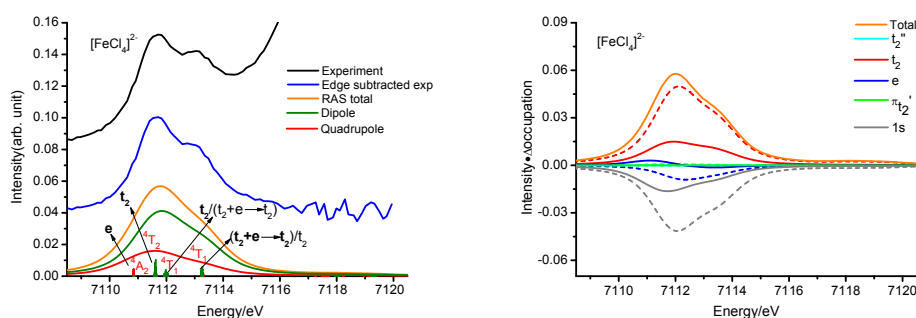


FIGURE 4.3: Left:Iron K pre-edge XAS of  $[FeCl_4]^{2-}$  showing experimental data (black), the edge-subtracted spectra (blue), and RAS results (total:orange, dipole:olive, quadrupole:red). Right:Orbital analyses for the K pre-edge XAS of  $[FeCl_4]^{2-}$ . Quadrupole contributions are denoted with solid lines while dipole contributions are shown with dashed lines.

The evident features of the K pre-edge for  $[FeCl_4]^{2-}$  are two intense peaks and are split by  $\sim 1.5$  eV.[39] For  $[FeCl_4]^{2-}$ , the  $^5E$  ground state has a  $e^3t_2^3$  configuration, electron transition to the  $e$  orbital gives the  $e^4t_2^3$  excited configuration and produces  $^4A_2$  state. The excited configuration  $e^3t_2^4$  gives  $^4T_1$  and  $^4T_2$  states due to the  $3d$ - $3d$  electron interactions, see Figure 4.3. Besides, there is a double-excitation state  $e^2t_2^4$  that gives another  $^4T_1$  located at higher energy region. The  $^4T_1$  states can mix, and the double excitations are also can be confirmed from our orbital contribution analysis, see Figure 4.3. These transitions form two pre-edge features split by 1.5 eV in the RAS calculation, which well reproduced the experimental split, see Table 4.1. The pre-edge energies have information about both ligand-field splitting and orbital covalency, but for a correct interpretation, the effects of configuration interaction with a doubly-excited state needs to be accounted for. DFT gave a splitting energy of  $\sim 0.7$  eV, which was significantly underestimated. The electric dipole transitions exist in excitations to  $t_2$  orbitals contributing to the total intensity of the K pre-edge, see Figure 4.3. Compared to the total intensity of  $[FeCl_6]^{4-}$ , the total intensity of  $[FeCl_4]^{2-}$  was largely increased. The RAS

calculated total intensity ratio between  $[FeCl_4]^{2-}$  and  $[FeCl_6]^{4-}$  is 3.2:1.0. The calculated intensity ratio between dipole and quadrupole for  $[FeCl_4]^{2-}$  is  $\sim 2.4:1$ . This is difficult to model using the semi-empirical CTM model because adding  $4p$  configurations significantly increases the number of fitting parameters. TD-DFT (BP86) includes the effects of orbital hybridization but overestimates the dipole contributions, at least for the current complexes modeled, see Figure 4.4

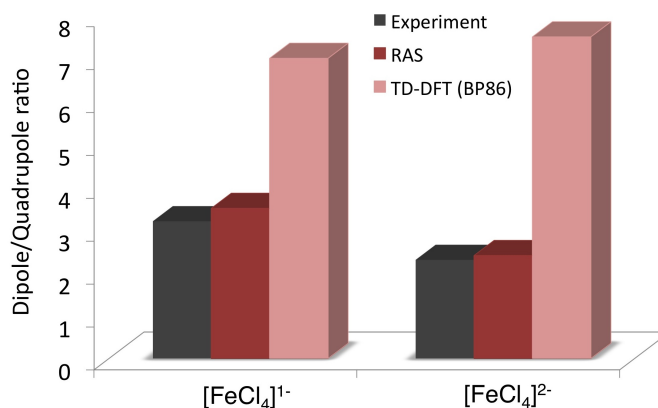


FIGURE 4.4: The ratio of dipole to quadrupole contributions to the pre-edge area from experiment, RAS and TD-DFT.

### 4.3 Back-donation charge transfer

$[Fe(CN)_6]^{3-}$  has been widely investigated as a  $\sigma$  donation and  $\pi$  back donation model system.[21, 70, 71] There are two peaks in the experimental K pre-edge of  $[Fe(CN)_6]^{3-}$  with intensity ratio of  $\sim 1:4.1$ , [39] see Figure 4.5. The energy difference between these two peaks is 3.2 eV, [39] which reflects the ligand-field strength, see Table 4.1. In the L-edge XAS, [21, 52, 70]  $[Fe(CN)_6]^{3-}$  has an intense peak that can be assigned to back-donation, see Section 3.2. However, it is not clear whether such features can be detected in K pre-edge spectra, as the back-donation transfer states are usually obscured by the rising edge. The edge-subtracted experimental K pre-edge also predicts another peak  $\sim 3.9$ eV higher than the  $e_g$  character peak. This means the charge transfer states still have important contributions to the K pre-edge, and it is necessary to describe the back-donation feature in the K pre-edge calculation.

The  ${}^2T_{2g}$  ground state of  $[Fe(CN)_6]^{3-}$  has a  $t_{2g}{}^5e_g{}^0$  configuration. A pre-edge peak located at lower energy side is present, which comes from  $1s$  electron excited into the singly occupied  $t_{2g}$  orbital, producing a  $t_{2g}{}^6e_g{}^0$  configuration and a  ${}^1A_{1g}$  state. Another excited configuration is  $t_{2g}{}^5e_g{}^1$  after  $1s$  electron excited into  $e_g$  orbital. The  $e_g$  peak is likely to contain a large contribution from multiplet effects due to the partially filled  $t_{2g}$

orbitals, which can complicate multiplet structures of final states through  $3d$ - $3d$  electron interactions. The interactions gave us  ${}^3T_{1g}$ ,  ${}^3T_{2g}$ ,  ${}^1T_{1g}$  and  ${}^1T_{2g}$  states, as labelled in the Figure 4.5. The difference in energy between the  $T_{1g}$  and  $T_{2g}$  states probe the difference in attraction between the hole in a  $d_{xy}$  orbital and the electron in the  $d_{z^2}$  compared to the  $d_{x^2-y^2}$ . The RAS calculations not only reproduced the 3.2-eV energy difference

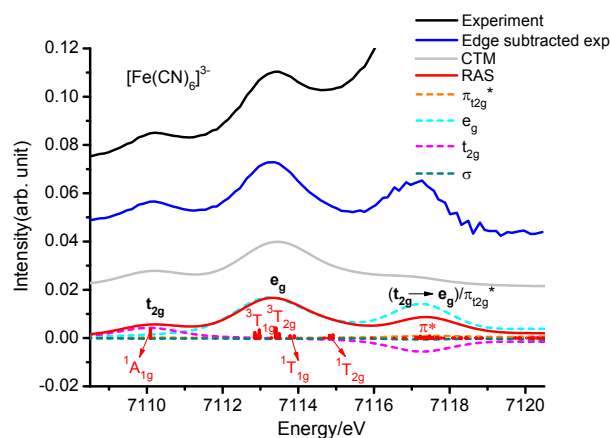


FIGURE 4.5: Iron K pre-edge XAS  $[Fe(CN)_6]^{3-}$  showing experimental data (black), the edge-subtracted spectra (blue), results from CTM calculations (light gray), and results from RAS calculations (red). Analyses of the valence orbital contributions are shown as dashed lines.

between the  $t_{2g}$  and  $e_g$  character peaks but also showed an intensity ratio of 1: 4.2 (1:4.1 for experimental result) for these two peaks. The CTM calculation had an energy difference between the  $t_{2g}$  and  $e_g$  character peaks of about 3.3 eV, and DFT gave a value of 3.5 eV. [30]

In addition to these two peaks, the RAS calculations showed a peak located at 4.0eV higher compared to the  $e_g$  character peak (1.9eV higher than the  ${}^1T_{2g}$  state), which was assigned to a  $\pi^*$  state. The intensity of the  $\pi^*$  state is high, although the contributions of direct excitation to  $\pi^*$  orbital is very small, as seen from the graphic orbital analysis, see Figure 4.5. The enhanced  $\pi^*$  feature comes from the direct  $\pi^*$  excitation mixes with a  $1s \rightarrow e_g + t_{2g} \rightarrow e_g$  shake-up excitation.[21, 70]. The  $\pi^*$  state was also predicted by the multiplet calculation using an extra electronic configuration  $t_{2g}^4 e_g^0$  including  $\pi$  back bonding. For the multiplet calculation, the  $\pi^*$  states located at 3.7 eV higher relative to the  $e_g$  character peak with a bit lower intensity compared to RAS calculation. The DFT gave a separation of  $\sim 1.6$ eV between  $e_g$  and MLCT states.[30]

## Chapter 5

# Simulation of the 1s2p RIXS

After successful application of the RAS method on L-edge and K pre-edge XAS simulations, it now is extended to simulate the 1s2p RIXS spectra. As we described in the introduction, the two-photon 1s2p RIXS process can reach the same final-state electron configuration as the L-edge absorption process, see Figure 1.3, and hence can give high-resolution X-ray spectra of transition metal complexes. In this chapter, the 1s2p RIXS spectra of back-donation systems  $[Fe(CN)_6]^{4-}$  and  $[Fe(CN)_6]^{3-}$  are simulated and discussed. The calculated and experimental 1s2p RIXS planes are presented in Figure 5.1, [21] which are plotted in a two-dimensional representation with energy transfer axis and incident energy axis.

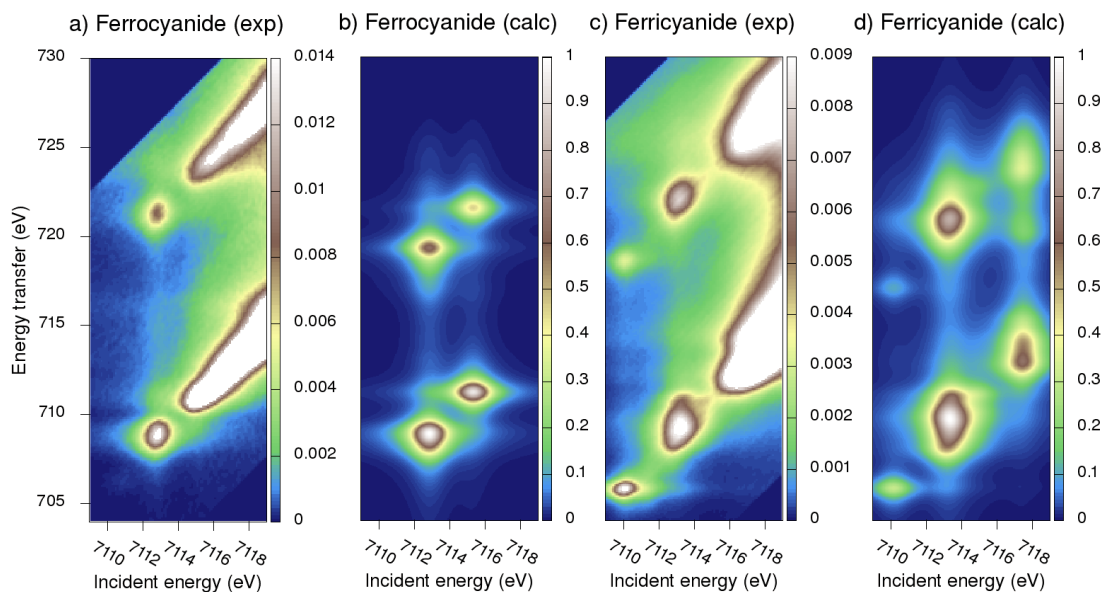


FIGURE 5.1: The calculated and experimental 1s2p RIXS plane of  $[FeCN_6]^{4-}$ .

## 5.1 The $1s2p$ RIXS spectrum of $[Fe(CN)_6]^{4-}$

In the experimental plane, there is one pre-edge resonance which can be assigned to  $1s \rightarrow e_g$  excitation, located at 7112.9 eV in the incident energy direction. The rising edge contributions include a peak at  $\sim 7115.5$  and other more intense peaks at higher energy,[21] see Figure 5.1. The calculated  $1s2p$  RIXS plane has same the general shape as the experimental plane, and exhibits a dominant resonance at 7112.9 eV with a second resonance at 7115.6 eV in the incident energy direction. The second resonance was assigned as a back-donation transition in the K pre-edge spectrum, which is obscured by the intense rising edge in the experimental plane.

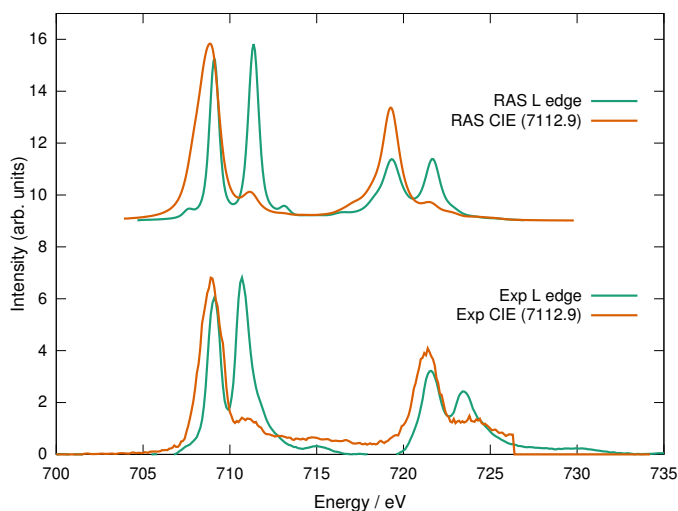


FIGURE 5.2: The L-edge XAS and CIE cut of  $[FeCN_6]^{4-}$ .

The  $1s2p$  RIXS spectrum was further analysed by taking a constant incident energy (CIE) cut giving an L-edge like spectrum, which can be directly compared to the L-edge XAS. The  $L_3$  edge of the L-edge XAS, has two peaks with similar intensity at  $\sim 709.1$  eV and  $\sim 710.7$  eV, which can be assigned to  $e_g$  and  $\pi^*$  excitation. The  $L_2$  edge also has these two peaks but with smaller intensities, see Figure 5.2.[70] A L-edge like spectrum was made by a CIE cut through the dominant resonance at 7112.9 eV. The L-edge like spectrum gives a broader  $e_g$  character peak and a very weak  $\pi^*$  character peak. The broader  $e_g$  peak in the L-edge like spectrum can be interpreted by the different transition selection rules for one- and two-photon processes. The  $2p^53d^7$  configuration final states have both  $T_{1u}$  and  $T_{2u}$  symmetry, but the one-photon L-edge XAS can only reach the  $T_{1u}$  final state while the two-photon RIXS can reach both  $T_{1u}$  and  $T_{2u}$  states. The excitation to a  $T_{2u}$  state give a lower energy because of more favorable  $2p - 3d$  electron interactions. The  $\pi^*$  character peak gave a weak intensity in the L-edge like spectrum because the final states corresponding to the  $\pi^*$  transitions are mainly reached through the intermediate states at  $\sim 7114.7$  eV, not the states at 7112.9 eV.[21]

The CIE cut from the RAS calculated RIXS spectrum nicely reproduces the spectral difference between RIXS and L-edge XAS, see Figure 5.2. Starting with the L-edge XAS, the RAS simulation is in excellent agreement with experiment, and the relative intensities of  $e_g$  and  $\pi^*$  peaks are very well described in the  $L_3$  edge. In the  $L_2$  edge, the  $e_g$  character peak is a little underestimated. In the CIE cut, the RAS calculation reproduces the change in the shape of the  $e_g$  resonance with additional intensity at the low-energy side. The width is 1.7 eV, an overestimation by 0.2 eV, which is a reasonable accuracy, see Figure 5.2. It has previously been suggested that the width of the  $e_g$  CIE peak is related to the metal-ligand covalency because it measures the relative interaction between a 2p hole localized on the metal and the 3d orbitals involved in bonding. The width of the CIE peak is slightly overestimated in RAS, and the  $e_g$  metal-ligand covalency of 65% metal content is also more ionic than reported for e.g., the density functional BP86 (57%) or the CTM model (45%).[55, 70]

## 5.2 The 1s2p RIXS spectrum of $[Fe(CN)_6]^{3-}$

The experimental 1s2p RIXS spectrum of  $[Fe(CN)_6]^{3-}$  gives several pre-edge features. The first sharp  $t_{2g}$  character resonance is located at  $\sim 7110.1$  eV. The second resonance is much broader and has a maximum at  $\sim 7113.3$  eV. This resonance is from  $1s \rightarrow e_g$  excitations, which are split into many different transitions by exchange, multiplet and spin-orbit interactions, as discussed in chapter 4.3, see Figure 4.5. The rising edge with its intense resonances is located at  $\sim 7117$  eV and above, see Figure 5.1. The RAS calculated RIXS plane contains both pre-edge peaks, and also a higher-lying  $\pi^*$  peak that appears as part of the rising edge.[52, 55, 70]

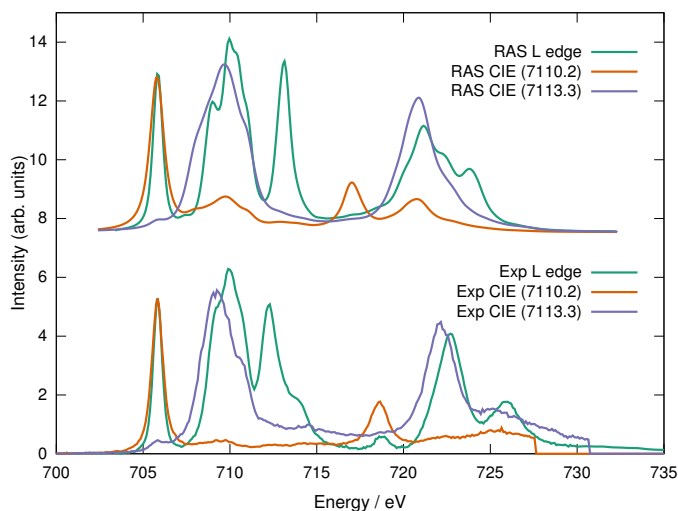


FIGURE 5.3: The L-edge XAS and CIE cut of  $[Fe(CN)_6]^{3-}$ .

The experimental and RAS calculated L-edge XAS are discussed in Section 3.2. The CIE cut through the RIXS  $t_{2g}$  resonance at 7110.1 eV gives two sharp edges, where the  $L_2$  peak is more intense than in the L-edge XAS. This is again due to differences in selection rules in RIXS compared to the L-edge, and this difference cannot be explained without a proper treatment of SOC. The CIE cut through the  $e_g$  resonance at 7113.3 eV shows a broad feature with a width of 2.7 eV in the  $L_3$  edge, see Figure 5.3.

Taking the RAS CIE cut through the  $t_{2g}$  correctly predicts the increase in intensity of the  $L_2$  edge in the two-photon process. This shows that the RAS method correctly takes into account the effects of  $3d$ , as well as  $2p$ , SOC in the RAS simulations. The CIE cut through the maximum of the  $e_g$  resonance is also in agreement with the experimental spectrum. As this resonance contains multiple pre-edge resonances, the CIE cuts are sensitive both to the incident and the emission energy, which makes it challenging to assign specific transitions. However, the agreement between RAS and experimental data shows that the RAS method can be used to connect a complicated spectrum to a detailed electronic structure model.

## Chapter 6

# Conclusion

In this thesis, the RAS method has been used to simulate and interpret the metal L-edges, K pre-edges and  $1s2p$  RIXS spectroscopies of different iron complexes. The experimental spectral features were well reproduced in the RAS simulations by including a high-level description of ligand-field, multiplet effects, spin-orbit coupling, as well as configuration interaction between different states.

More specifically, in the case of  $[FeCl_6]^{4-}$ , the K pre-edge XAS is complicated by multiplet effects and the mixing of final states sharing the same symmetry, and this all well described in the RAS calculation. The distortion from centrosymmetry by changing the coordination number can give arise electric dipole transitions in the K pre-edge region due to  $3d - 4p$  orbital hybridization. Here  $[FeCl_4]^{2-}$  is taken as an example to disentangle intensity mechanisms. The intensity ratio has been calculated correctly, giving  $\sim 2.4:1$  compared to  $\sim 2.3:1$  in experiment. It is essential to be able to estimate the dipole contributions to correctly predict spectral effects when a catalyst site changes during a reaction. The back-donation charge transfer feature of  $[Fe(CN)_6]^{3-}$  is observable in both metal L-edge and K pre-edge XAS, and they are all nicely reproduced in RAS calculations. The extension of the RAS approach to  $1s2p$  RIXS calculations has also been implemented and tested for  $[Fe(CN)_6]^{4-}$  and  $[Fe(CN)_6]^{3-}$ . The RAS method gives good description of  $3d - 3d$  interactions and  $3d$  SOC along incident energy axis, and the  $2p - 3d$  interaction and  $2p$  SOC along the energy transfer axis. The two-photon spectroscopy provides ample electronic structural information of ground and excited states, which make it has great potential to directly probe dilute enzymatic systems and working catalysts.

The orbital contribution analysis of the X-ray spectra based on the RAS calculation enables a direct connection between spectra and the electronic structure features. The

RAS method can therefore be of great use in the interpretation of a wide variety of different X-ray experiments.

## *Acknowledgements*

First and foremost I would like to express gratitude to my supervisor, **Marcus Lundberg**, for guiding me to the field of X-ray spectroscopy, for his supporting and care. I really enjoyed and learned a lot from our every discussion and meeting, thanks very much for your remarkable patience.

Thanks my co-supervisor and the group leader **Roland Lindh**, for his dedication to build positive, creative and loving working environment, make us work and get along as a team, even family.

I would like to appreciate the former postdoc **Rahul V. Pinjari**, who helped me a lot when I started my PhD project, and shared his knowledge and experience in doing X-ray study.

I thank **Ignacio Fernández**, 'The Fika Envoy', for bringing us to leisure, and also for your help with Molcas and Latex program.

Thanks **Pooria Farahani**, Shifu of swimming, for your encouraging words, the painful and scary memory of diving from ten-meters platform dwarfs the dark side of PhD life.

Thanks the collaboration with **Philippe Wernet** and **Markus Kubin** from BESSY II, the collaboration triggered my interest in the the X-ray experiment.

I also grateful to all the former and present member at the theoretical chemistry programme, **Liqin Xue**, **Natasha kamerlin**, **Michael Stenrup**, **Charlotta Bengtson**, **Hans Karlsson**, **Dennis Caldwell**, **Nessima Salhi**, **Orlando Tapia**, **Lasse Kragh Sørensen**, **Mickaël G Delcey**, **Erik Källman**, **Martin Agback**, **Esko Makkonen**, **Piotr Froelich**, and many others.

A warm thank you to **Cici** and **Yohan**, for the licentiate shirt gift, and for your company of two Christmas holidays.

And finally, thanks my family, for infinite understanding and supporting all the time.



# Bibliography

- [1] Nicola Armaroli and Vincenzo Balzani. *Angew. Chem., Int. Ed.*, 46(1-2):52–66, 2007.
- [2] Tomoji Kawai and Tadayoshi Sakata. *Nature.*, 286:474–476, 1980.
- [3] Nathan S Lewis and Daniel G Nocera. *Proc. Nat. Acad. Sci. USA.*, 103(43):15729–15735, 2006.
- [4] James Barber. *Chem. Soci. Rev.*, 38(1):185–196, 2009.
- [5] Akihiko Kudo and Yugo Miseki. *Chem. Soc. Rev.*, 38(1):253–278, 2009.
- [6] Kazuhiko Maeda and Kazunari Domen. *J. Phys. Chem. Lett.*, 1(18):2655–2661, 2010.
- [7] Pingwu Du and Richard Eisenberg. *Energ. Environ. Sci.*, 5(3):6012–6021, 2012.
- [8] Vincent Artero, Murielle Chavarot-Kerlidou, and Marc Fontecave. *Angew. Chem., Int. Ed.*, 50(32):7238–7266, 2011.
- [9] Ward Jesse, Ollmann Emily, Maxey Evan, and A. Finney. Lydia. *X-Ray Absorption Spectroscopy of Metalloproteins*. Humana Press: Springer, New York, NY(USA), 2014.
- [10] Junko Yano and Vittal K Yachandra. *Photosynth. Res.*, 102(2-3):241–254, 2009.
- [11] Pieter Glatzel, Uwe Bergmann, Junko Yano, Hendrik Visser, John H Robblee, Weiwei Gu, Frank MF de Groot, George Christou, Vincent L Pecoraro, Stephen P Cramer, and Vital K. Yachandra. *J. Am. Chem. Soc.*, 126(32):9946–9959, 2004.
- [12] Kari L Stone, Rachel K Behan, and Michael T Green. *Proc. Nat. Acad. Sci. USA.*, 102(46):16563–16565, 2005.
- [13] Junko Yano and Vittal Yachandra. *Chem. Rev.*, 114(8):4175–4205, 2014.
- [14] Serena DeBeer George, Patrick Brant, and Edward I Solomon. *J. Am. Chem. Soc.*, 127(2):667–674, 2005.
- [15] Takashi Yamamoto. *X-Ray. Spectrom.*, 37(6):572–584, 2008.
- [16] AL Roe, DJ Schneider, RJ Mayer, JW Pyrz, J Widom, and L Que Jr. *J. Am. Chem. Soc.*, 106(6):1676–1681, 1984.
- [17] Jan-Uwe Rohde, Theodore A Betley, Timothy A Jackson, Caroline T Saouma, Jonas C Peters, and Lawrence Que. *Inorg. Chem.*, 46(14):5720–5726, 2007.
- [18] Manfred Otto Krause and JH Oliver. *J. Phys. Chem. Ref. Data.*, 8(2):329–338, 1979.

- [19] Pieter Glatzel and Uwe Bergmann. *Coordin. Chem. Rev.*, 249(1):65–95, 2005.
- [20] P Glatzel, M Sikora, and Marcos Fernández-García. *Euro. Phys. J. Spec. Top.*, 169(1):207–214, 2009.
- [21] Marcus Lundberg, Thomas Kroll, Serena DeBeer George, Uwe Bergmann, Samuel A Wilson, Pieter Glatzel, Dennis Nordlund, Britt Hedman, Keith O Hodgson, and Edward I Solomon. *J. Am. Chem. Soc.*, 135(45):17121–17134, 2013.
- [22] Thomas Kroll, Ryan G Hadt, Samuel A Wilson, Marcus Lundberg, James J Yan, Tsu-Chien Weng, Dimosthenis Sokaras, Roberto Alonso-Mori, Diego Casa, Mary H Upton, et al. *J. Am. Chem. Soc.*, 136(52):18087–18099, 2014.
- [23] Luuk JP Ament, Michel van Veenendaal, Thomas P Devereaux, John P Hill, and Jeroen van den Brink. *Rev. Mod. Phys.*, 83(2):705, 2011.
- [24] Y Joly. *Phys. Rev. B*, 63(12):125120, 2001.
- [25] John J Rehr, Joshua J Kas, Fernando D Vila, Micah P Prange, and Kevin Jorissen. *Phys. Chem. Chem. Phys.*, 12(21):5503–5513, 2010.
- [26] L Triguero, LGM Pettersson, and H Ågren. *Phys. Rev. B*, 58(12):8097, 1998.
- [27] J Vinson, JJ Rehr, JJ Kas, and EL Shirley. *Phys. Rev. B.*, 83(11):115106, 2011.
- [28] Andris Gulans, Stefan Kontur, Christian Meisenbichler, Dmitrii Nabok, Pasquale Pavone, Santiago Rigamonti, Stephan Sagmeister, Ute Werner, and Claudia Draxl. *J. Phys.-Condens. Mat.*, 26(36):363202, 2014.
- [29] Ulf Ekström, Patrick Norman, Vincenzo Carravetta, and Hans Ågren. *Phys. Rev. Lett.*, 97(14):143001, 2006.
- [30] Serena DeBeer George, Taras Petrenko, and Frank Neese. *J. Phys. Chem. A.*, 112(50):12936–12943, 2008.
- [31] Arto Sakko, Angel Rubio, Mikko Hakala, and Keijo Hämäläinen. *J. Chem. Phys.*, 133(17):174111, 2010.
- [32] P Chandrasekaran, S Chantal E Stieber, Terrence J Collins, Lawrence Que Jr, Frank Neese, and Serena DeBeer George. *Dalton. T.*, 40(42):11070–11079, 2011.
- [33] Frederico A Lima, Ragnar Bjornsson, Thomas Weyhermüller, Perumalreddy Chandrasekaran, Pieter Glatzel, Frank Neese, and Serena DeBeer George. *Phys. Chem. Chem. Phys.*, 15(48):20911–20920, 2013.
- [34] G Capano, TJ Penfold, NA Besley, CJ Milne, M Reinhard, H Rittmann-Frank, P Glatzel, R Abela, U Rothlisberger, M Chergui, et al. *Chem. Phys. Lett.*, 580:179–184, 2013.
- [35] Michael Roemelt, Dimitrios Maganas, Serena DeBeer, and Frank Neese. *J. Chem. Phys.*, 138(20):204101, 2013.
- [36] Dimitrios Maganas, Michael Roemelt, Thomas Weyhermüller, Raoul Blume, Michael Hävecker, Axel Knop-Gericke, Serena DeBeer, Robert Schlögl, and Frank Neese. *Phys. Chem. Chem. Phys.*, 16(1):264–276, 2014.

- [37] M-A Arrio, S Rossano, Ch Brouder, L Galois, and G Calas. *Europhys. Lett.*, 51(4):454, 2000.
- [38] Frank MF de Groot. *Coordin. Chem. Rev.*, 249(1):31–63, 2005.
- [39] Tami E Westre, Pierre Kennepohl, Jane G DeWitt, Britt Hedman, Keith O Hodgson, and Edward I Solomon. *J. Am. Chem. Soc.*, 119(27):6297–6314, 1997.
- [40] Björn O Roos, Peter R Taylor, Per EM Si, et al. *Chem. Phys.*, 48(2):157–173, 1980.
- [41] Björn O Roos. *Adv. Chem. Phys.*, pages 399–445, 1987.
- [42] Jeppe Olsen, Björn O Roos, Poul Jorgensen, and Hans Jorgen Aa. Jensen. *J. Chem. Phys.*, 89(4):2185–2192, 1988.
- [43] Kerstin Andersson, Per-Åke Malmqvist, Björn O Roos, Andrzej J Sadlej, and Krzysztof Wolinski. *J. Phys. Chem.*, 94(14):5483–5488, 1990.
- [44] Kerstin Andersson, Per-Åke Malmqvist, and Björn O Roos. *J. Chem. Phys.*, 96(2):1218–1226, 1992.
- [45] Per Åke Malmqvist, Kristine Pierloot, Abdul Rehaman Moughal Shahi, Christopher J Cramer, and Laura Gagliardi. *J. Chem. Phys.*, 128(20):204109, 2008.
- [46] Per Åke Malmqvist, Alistair Rendell, and Björn O Roos. *J. Phys. Chem.*, 94(14):5477–5482, 1990.
- [47] Ida Josefsson, Kristjan Kunnus, Simon Schreck, Alexander Fohlich, Frank de Groot, Philippe Wernet, and Michael Odelius. *J. Phys. Chem. Lett.*, 3(23):3565–3570, 2012.
- [48] Philippe Wernet, Kristjan Kunnus, Simon Schreck, Wilson Quevedo, Reshmi Kurian, Simone Techert, Frank MF de Groot, Michael Odelius, and Alexander Fohlich. *J. Phys. Chem. Lett.*, 3(23):3448–3453, 2012.
- [49] Sergey I Bokarev, Marcus Dantz, Edlira Suljoti, Oliver Kühn, and Emad F Aziz. *Phys. rev. Lett.*, 111(8):083002, 2013.
- [50] Kaan Atak, Sergey I Bokarev, Malte Gotz, Ronny Golnak, Kathrin M Lange, Nicholas Engel, Marcus Dantz, Edlira Suljoti, Oliver Kuhn, and Emad F Aziz. *J. of Phys. Chem. B.*, 117(41):12613–12618, 2013.
- [51] Nicholas Engel, Sergey I Bokarev, Edlira Suljoti, Raul Garcia-Diez, Kathrin M Lange, Kaan Atak, Ronny Golnak, Alexander Kothe, Marcus Dantz, Oliver Kuhn, et al. *J. Phys. Chem. B.*, 118(6):1555–1563, 2014.
- [52] Rahul V Pinjari, Mickaël G Delcey, Meiyuan Guo, Michael Odelius, and Marcus Lundberg. *J. Chem. Phys.*, 141(12):124116, 2014.
- [53] Ph Wernet, K Kunnus, I Josefsson, I Rajkovic, W Quevedo, M Beye, S Schreck, S Grübel, M Scholz, D Nordlund, et al. *Nature*, 520(7545):78–81, 2015.
- [54] Rahul V Pinjari, Mickaël G Delcey, Meiyuan Guo, Michael Odelius, and Marcus Lundberg. *J. Comput. Chem.*, 37:477486, 2016.
- [55] Meiyuan Guo, Lasse Kragh Sørensen, Mickaël G Delcey, Rahul V Pinjari, and Marcus Lundberg. *Phys. Chem. Chem. Phys.*, 18(4):3250–3259, 2016.
- [56] Max Born and Robert Oppenheimer. *Annalen der Physik*, 389(20):457–484, 1927.

- [57] Charlotte Froese Fischer. *Comput. phys. commun.*, 43(3):355–365, 1987.
- [58] Per-Olov Löwdin. *Phys. rev.*, 97(6):1509, 1955.
- [59] James Finley, Per-Åke Malmqvist, Björn O Roos, and Luis Serrano-Andrés. *Chem. phys. lett.*, 288(2):299–306, 1998.
- [60] Per Åke Malmqvist, Björn O Roos, and Bernd Schimmelpfennig. *Chem. phys. lett.*, 357(3):230–240, 2002.
- [61] Marvin Douglas and Norman M Kroll. *Ann of Phys*, 82(1):89–155, 1974.
- [62] Björn O Roos, Roland Lindh, Per-Åke Malmqvist, Valera Veryazov, and Per-Olof Widmark. *J. Phys. Chem. A.*, 108(15):2851–2858, 2004.
- [63] Björn O Roos, Roland Lindh, Per-Åke Malmqvist, Valera Veryazov, and Per-Olof Widmark. *J. Phys. Chem. A.*, 109(29):6575–6579, 2005.
- [64] Francesco Aquilante, Thomas Bondo Pedersen, and Roland Lindh. *J. Chem. Phys.*, 126(19):194106, 2007.
- [65] Francesco Aquilante, Per-Åke Malmqvist, Thomas Bondo Pedersen, Abhik Ghosh, and Björn Olof Roos. *J. Chem. Theory. Comput.*, 4(5):694–702, 2008.
- [66] Per-Åke Malmqvist and Björn O Roos. *Chem. Phys. Lett.*, 155(2):189–194, 1989.
- [67] Stephan Bernadotte, Andrew J Atkins, and Christoph R Jacob. *J. Chem. Phys.*, 137(20):204106, 2012.
- [68] Hendrik A Kramers and Werner Heisenberg. *Zeitschrift für Physik A Hadrons and Nuclei*, 31(1):681–708, 1925.
- [69] Sergey I Bokarev, Munirah Khan, Mahmoud K Abdel-Latif, Jie Xiao, Rifaat Hilal, Saadullah G Aziz, Emad F Aziz, and Oliver Kuhn. *J. Phys. Chem. C.*, 119(33):19192–19200, 2015.
- [70] Rosalie K Hocking, Erik C Wasinger, Frank MF de Groot, Keith O Hodgson, Britt Hedman, and Edward I Solomon. *J. Am. Chem. Soc.*, 128(32):10442–10451, 2006.
- [71] Rosalie K Hocking, Erik C Wasinger, Yi-Long Yan, Frank MF deGroot, F Ann Walker, Keith O Hodgson, Britt Hedman, and Edward I Solomon. *J. Am. Chem. Soc.*, 129(1):113–125, 2007.